Wetter, weaker, and more frequent monsoon low-pressure systems in CMIP6 future scenarios

Wetter, Weaker, and More Frequent Monsoon Low Pressure Systems in CMIP6 Future Scenarios

KIERAN M. R. HUNT[a,b] AND ANDREW G. TURNER[a,b]

[a] *Department of Meteorology, University of Reading, Reading, United Kingdom*
[b] *National Centre for Atmospheric Sciences, University of Reading, Reading,United Kingdom*

(Manuscript received 7 July 2025, in final form 18 September 2025, accepted 7 November 2025)

ABSTRACT: The South Asian monsoon is strongly influenced by synoptic-scale low pressure systems (LPSs), which deliver the majority of seasonal and extreme rainfall. Here, we provide a robust synthesis of future LPS characteristics by analyzing 13 models from the Coupled Model Intercomparison Project phase 6 (CMIP6). We develop a novel, multicomponent skill score (FLIP: frequency, location, intensity, and precipitation) to evaluate and weight model performance against reanalysis benchmarks. Our weighted multimodel projections reveal a consistent narrative for future monsoons: LPSs are projected to become more frequent and dynamically weaker in terms of low-level vorticity as global warming levels increase. Per-LPS precipitation is projected to increase, with a super Clausius–Clapeyron scaling for the most intense storms, despite a general weakening of their circulation. We attribute this apparent paradox to a projected increase in the background meridional moisture gradient and a structural change whereby boundary layer winds weaken less than those in the free troposphere, maintaining strong frictional moisture convergence. Furthermore, LPSs are projected to penetrate deeper inland, with a significant increase in postlandfall duration between 1.5° and 2°C of warming. To deconstruct intermodel uncertainty, we employ a storyline approach based on unsupervised clustering of circulation and moisture anomalies. This reveals four physically self-consistent yet distinct future pathways that explain model diversity in LPS frequency, track, and precipitation changes. For example, a storyline with enhanced easterlies over Southeast Asia leads to a 36% increase in LPS frequency by transporting more precursor disturbances into the Bay of Bengal. Averaging over these diverse futures, the consistent outcome is a monsoon dominated by more numerous and wetter LPSs that track deeper into the subcontinent, expanding the risk of extreme rainfall and flooding to western parts of India.

KEYWORDS: Monsoons; Storm tracks; Synoptic-scale processes; Storm environments

1. Introduction

a. Climate change and the South Asian monsoon

The South Asian monsoon is associated with significant multidecadal variability, present in both long instrumental records (Sontakke et al. 2008) and multicentennial paleoclimate reconstructions (Shi et al. 2018; Hunt and Harrison 2025). This is thought mostly to arise from teleconnections with the Atlantic multidecadal variability and Pacific decadal variability (Jiang and Zhou 2019).

In the last century, anthropogenic climate change has started to dominate this interdecadal variability. Global monsoon rainfall decreased from 1950 until about 1990, largely due to aerosols, before rebounding after 1990 as the effect of warming from increasing greenhouse gases began to dominate (Wang et al. 2021). Over South Asia, this inflection point occurred slightly later, in about 2000 (Kitoh et al. 2013; Doblas-Reyes et al. 2021) Bollasina et al. (2011) showed that aerosol loading reduces monsoon rainfall over India through, in part, weakening the land–ocean temperature gradient.

Despite this, there is high confidence among model projections that continued global warming will lead to an increase in both mean and extreme monsoon precipitation in the future (Chen et al. 2020; Wang et al. 2020; Moon and Ha 2020; Katzenberger et al. 2021; Wang et al. 2021), with increased variability across a range of scales. This increase arises from the Clausius–Clapeyron relationship, wherein an increase in air temperature of 1 K increases its corresponding saturation vapor pressure by 7%. Monsoon precipitation is not projected to increase quite this rapidly (i.e., sub-CC), however, as the underlying lower-tropospheric circulation, and hence the overturning circulation, is projected to weaken due to reduced meridional temperature gradients (Held and Soden 2006; Kitoh et al. 2013).

The projected precipitation trend has a zonal gradient, with a greater increase over west India than east India, a pattern that has already been identified in observations (Kumari et al. 2025).

b. Monsoon low pressure systems

As monsoon low pressure systems (LPSs) are responsible for the majority of both mean and extreme monsoon precipitation (Hunt and Fletcher 2019; Thomas et al. 2021; Suhas et al. 2023), it is reasonable to assume that the projected changes to monsoon precipitation will be mediated through them.

Earlier studies that have used LPS tracks to create storm-centered composite fields have given us a complete picture of

Denotes content that is immediately available upon publication as open access.

Corresponding author: Kieran M. R. Hunt, k.m.r.hunt@reading.ac.uk

DOI: 10.1175/JCLI-D-25-0389.1

the mean LPS structure and thermodynamics (Godbole 1977; Stano et al. 2002; Hurley and Boos 2015; Hunt et al. 2016a,b). A warm core aloft is supported by latent heating from both synoptic-scale and convective-scale moist updrafts. This supports a broad, deep, and dense cloud structure as well as widespread heavy precipitation with a maximum usually to the southwest of the center.

Between 30% and 60% of LPSs spin up from precursor vortices that can be tracked as far back as Southeast Asia, the South China Sea, or the west Pacific (Saha et al. 1981; Chen and Weng 1999; Meera et al. 2019). Regional climate models fed with climatological (i.e., nonvarying) boundary conditions substantially underestimate LPS frequency, implying the importance of initial disturbances (or "seeds") originating from outside the Bay of Bengal (Levine and Martin 2018). The remaining LPSs arise from dynamic instability at the western end of the monsoon trough and as such are frequently triggered by the boreal summer intraseasonal oscillation (BSISO) (Hunt and Turner 2022). Srujan et al. (2021) showed that Coupled Model Intercomparison Project phase 5 (CMIP5) models simulated this partition reasonably well, with 30% of systems they tracked having genesis outside of the Indian basins.

The question of how LPSs intensify within the monsoon environment has been long debated. Earlier studies proposed barotropic and moist baroclinic modes (e.g., Goswami et al. 1980; Moorthi and Arakawa 1985; Rajamani and Sikdar 1989). However, recent studies based on idealized model experiments have made a compelling case in support of growth through moist barotropic instability, i.e., a coupling of convection to the large-scale background meridional gradient in zonal wind (Diaz and Boos 2019, 2021; Suhas and Boos 2023). In parallel, Adames and Ming (2018) and Adames (2021) developed the "moisture vortex" instability theory, where vortex growth is supported directly by convection. Recent attempts to unify these theories have shown that both are important for LPS growth, with moisture-vortex instability needed to explain precipitation phasing and growth from MSE gradients and barotropic instability to explain peak LPS intensity (Luo et al. 2023; Hunt and Turner 2024).

In contrast, relatively little research has focused on processes governing LPS decay, despite this being an important control on the time that LPSs spend over land, and therefore how much precipitation they contribute to the monsoon. Those studies that have explored LPS decay and inland penetration stress the importance of land surface conditions, either directly through soil moisture (Kishtawal et al. 2013; Hunt and Turner 2017; Deoras et al. 2025) or indirectly through surface fluxes (Chang et al. 2009).

c. *LPSs and climate change*

Observational studies on long-term trends of monsoon LPS frequency have typically derived from the track catalogue compiled manually by Sikka (2006) or the catalogue of depressions—the stronger variety of LPSs—tracked manually and maintained pseudo-operationally by the India Meteorological Department. Such studies have typically reported negative trends in depressions but an increase in nondepression LPSs, usually referred to as "lows" (Prajeesh et al. 2013; Dash et al. 2004; Vishnu et al. 2016). Studies that have used LPS tracks derived objectively from reanalyses have found no significant trend in either depressions (Cohen and Boos 2014) or lows (Vishnu et al. 2020) over the last 50 years. Vishnu et al. (2020) noted strong modulation in frequency by ENSO, as had been reported previously (Krishnamurthy and Ajayamohan 2010), suggesting that there may be significant interdecadal variability as well. You and Ting (2021) used a similar approach and while they did not report a trend in frequency, they found a significant trend in track density, with LPSs in recent years more likely to be found further south than previously, over central India, and have deeper inland penetration.

Previous studies have also explored LPS-related trends in climate models, typically using one or several CMIP-class GCMs (Rastogi et al. 2018; Sandeep et al. 2018; Dong et al. 2020; Thomas et al. 2022b; Vishnu et al. 2023). These studies all agree that future global warming will lead to an increase in per-LPS precipitation and a reduction in LPS activity (i.e., more lows at the expense of fewer depressions, or fewer systems overall). These are attributed to Clausius–Clapeyron scaling and a weakening of the overall monsoon circulation, respectively. Additionally, Rastogi et al. (2018) and Thomas et al. (2022b) reported a projected increase in associated extreme precipitation. In a pseudo–global warming experiment, Sørland et al. (2016) found a super-CC response of 13% K^{-1} for LPS precipitation, as well as a significant increase in LPS intensity. Such experiments, however, only reflect local changes in thermodynamics and do not necessarily capture the broader circulation changes (e.g., weakening monsoon).

These changes occur alongside projected shifts in LPS track density. While studies agree that this likely means a significant decline in track density over the Bay of Bengal, they disagree on exactly what happens elsewhere. Sandeep et al. (2018) reported that LPSs would shift slightly poleward, Dong et al. (2020) reported an increase in track density over central India, whereas Vishnu et al. (2023) found that LPSs would shift both to the north and south (i.e., widening their region of impact). That the studies agree on trends in precipitation and intensity but disagree on track density points to the complicated relationship between large-scale circulation, LPS genesis, and LPS propagation.

GCMs are not without their biases, either. These include the representation of monsoon circulation being too weak, with a resulting dry bias over central India (Sperber et al. 2013), LPS track density being too far north (Dong et al. 2020; Thomas et al. 2022a), and intraseasonal variability being too weak (Abatan et al. 2021; Konda and Vissa 2022), which could have a profound impact on the representation of LPS variability (Hunt and Turner 2022).

Clearly, then, a more robust approach is required to better quantify future changes to LPS statistics. Such an approach must account both for model bias and intermodel diversity. Therefore, in this paper, we propose the following:

1) Develop a score for individual CMIP6 models measuring their ability to simulate LPSs across a range of metrics.

2) Use this score as a weight for multimodel means, better quantifying future changes in LPS statistics as functions of global warming level.
3) Understand these changes through composites of LPS structure and storyline-based approaches.

We discuss the data and methods used in sections 2 and 3, respectively. Our results section is split into four parts: model evaluation (section 4a, overall trends in LPS characteristics (section 4b), then explaining these trends through composite analysis of LPS structure (section 4c), and storylines (section 4d). We then discuss the implications and shortcomings of our results in section 5 before concluding in section 6.

2. Data

a. ERA5

To assess CMIP6 model skill in the historical period, we use two reanalysis benchmarks. The first of these is the ECMWF ERA5 reanalysis (Hersbach et al. 2020). Data are available globally, at hourly resolution from 1940 onward, on a 0.25° grid. Data are available over 37 pressure levels from 1000 to 0.01 hPa, as well as at or near the surface. Data are assimilated into the forecasting system from a large variety of sources, including satellites, automatic weather stations, and radiosondes. Data were downloaded using the dedicated application programming interface (API) from the online source (https://cds.climate.copernicus.eu/cdsapp#!/dataset/reanalysis-era5-pressure-levels). We use 850-hPa vorticity to track LPSs and measure their intensity, as well as surface precipitation data to compute LPS rainfall. In studies comparing the quality of rainfall datasets over India and during the summer monsoon, ERA5 has been found to be highly skillful (e.g., Mahto and Mishra 2019; Bhattacharyya et al. 2022; Paul and Alemohammad 2025).

b. MERRA-2

The second reanalysis benchmark is the Modern-Era Retrospective Analysis for Research and Applications, version 2 (MERRA-2; Gelaro et al. 2017). MERRA-2 is a global atmospheric reanalysis dataset produced by NASA. It spans from 1980 to the present at a resolution of 0.625° × 0.5°. It has 42 pressure levels ranging from 1000 to 0.1 hPa at an hourly output frequency. Like ERA5, data are assimilated frequently and from a wide range of sources. Data were downloaded from the NASA website (https://disc.gsfc.nasa.gov/datasets?project=MERRA-2). Vorticity is computed from u and v winds at the 850-hPa level.

c. CMIP6

In this study, we use CMIP6 (Eyring et al. 2016) climate models whose pressure-level output is freely available at 6-hourly frequency (required to track LPSs) on the Centre for Environmental Data Analysis (CEDA) archive. A list of these models is given in Table 1. We use output from the preindustrial control runs (several centuries using preindustrial radiative forcing), the historical runs (typically 1850–2015; using observed greenhouse gases and aerosols), and the shared socioeconomic pathway (SSP) runs (typically 2015–2100 with a range of projected greenhouse gas and aerosol emissions). Not all SSPs are available in all models, but we use all that are available for any given model, namely, SSP119, SSP126, SSP245, SSP370, and SSP585. For more information on these configurations, the reader is referred to O'Neill et al. (2016). For model evaluation, we only require data to be available for the historical experiment, giving a total of 31 models. However, for the future climate change analysis, we also require 6-hourly data for both the historical experiment and at least one future scenario. This leaves us with a total of 13 models, marked with an asterisk in Table 1. For each model, we use only the first ensemble member (typically r1i1p1f1).

For tracking LPSs, we use 6-hourly vorticity data, which we compute from the u and v wind components. For per-LPS precipitation, we use accumulated 6-hourly precipitation data where available, sometimes constructed from two 3-hourly precipitation accumulations. If these data are unavailable, we do not track LPSs in that model-scenario.

d. Large ensembles

We also make use of two large ensembles, MIROC6 LE and MPI-ESM1-2-LR LE. These are single-model "superensembles" in which dozens of integrations are run with the same forcings but different initial conditions. Because the only difference between members is the initialization, the spread across the ensemble samples the model's internal climate variability. We use these to quantify the role of internal variability in driving changes to LPS statistics as compared to intermodel and interscenario variability. Although dozens of ensemble members are produced, only a handful were available to us with the required 6-hourly resolution. As such, we present the framework regardless, noting that our results are subject to a small sample size. There are three members available for each model scenario.

3. Methods

a. LPS tracking

To track LPSs in reanalysis and climate model data, we use a modification of the vorticity-based algorithm described in Hunt and Fletcher (2019).

1) We compute 850-hPa relative vorticity at 6-hourly intervals using u and v wind data for June–September. For ERA5, relative vorticity is already available on pressure levels, so this step is not required.
2) We apply a T63 spectral truncation to the vorticity data to filter out short-wavelength noise.
3) We identify regions of positive relative vorticity within this field and determine the centroid location for each one. The centroid is defined as the "center of mass," i.e., the vorticity-weighted average location of points in the region.
4) We link these centroids in time to form candidate LPS tracks. These are subject to constraints in distance: The algorithm searches for the next centroid starting at the location predicted by the mean LPS propagation vector for its previous position (typically northwestward). If no points

TABLE 1. FLIP scores for the 31 climate models and two reanalyses used in this study (ECMWF_ERA5 is the reference), evaluated over 1940–2015 except for MERRA-2 (1980–2015). Bold indicates the five highest-scoring models in each column, including the total score. Asterisks indicate those models used in the future climate analysis part of this study.

	FLIP score				
Model code	Frequency	Location	Intensity	Precip	Total
AS-RCEC_TaiESM1	0.142	0.553	**0.938**	**0.942**	0.644
AWI_AWI-ESM-1-1-LR	0.075	0.274	0.864	0.620	0.458
BCC_BCC-CSM2-MR*	0.007	0.432	0.442	0.445	0.332
CMCC_CMCC-CM2-HR4	**0.651**	0.654	0.844	**0.912**	**0.765**
CMCC_CMCC-CM2-SR5	0.048	0.414	0.897	**0.892**	0.563
CNRM-CERFACS_CNRM-CM6-1-HR	**0.712**	0.760	0.652	0.709	**0.708**
CSIRO-ARCCSS_ACCESS-CM2*	0.002	0.707	**0.904**	0.741	0.588
CSIRO_ACCESS-ESM1-5	0.000	0.592	**0.940**	0.633	0.541
EC-Earth-Consortium_EC-Earth3-AerChem	0.027	0.753	0.803	0.797	0.595
EC-Earth-Consortium_EC-Earth3-Veg-LR	0.003	0.732	0.794	0.732	0.566
EC-Earth-Consortium_EC-Earth3*	0.003	0.728	0.810	0.745	0.572
IPSL_IPSL-CM5A2-INCA	0.000	0.094	0.554	0.510	0.289
IPSL_IPSL-CM6A-LR-INCA	0.000	0.266	0.650	0.770	0.422
IPSL_IPSL-CM6A-LR	0.000	0.233	0.616	0.772	0.405
KIOST_KIOST-ESM*	0.280	0.762	0.704	0.581	0.582
MIROC_MIROC-ES2L	0.029	0.351	0.677	0.866	0.481
MIROC_MIROC6*	**0.432**	0.749	0.829	0.634	0.661
MOHC_HadGEM3-GC31-LL	0.033	**0.824**	**0.955**	0.810	0.655
MOHC_HadGEM3-GC31-MM*	0.129	**0.879**	0.878	0.839	**0.681**
MOHC_U.K.ESM1-0-LL*	0.053	**0.767**	0.903	0.870	0.648
MPI-M_MPI-ESM1-2-HR	0.104	0.410	0.836	0.764	0.529
MPI-M_MPI-ESM1-2-LR*	0.045	0.322	**0.947**	0.729	0.511
MRI_MRI-ESM2-0*	0.004	0.759	0.894	0.838	0.624
NASA-GISS_GISS-E2-1-G	0.113	0.190	0.678	0.540	0.380
NCC_NorESM2-LM*	0.017	0.450	0.821	**0.911**	0.550
NCC_NorESM2-MM*	0.359	**0.773**	0.827	**0.934**	**0.723**
NIMS-KMA_KACE-1-0-G*	0.007	0.690	0.841	0.857	0.599
NOAA-GFDL_GFDL-CM4	**0.481**	0.531	0.863	0.829	0.676
NOAA-GFDL_GFDL-ESM4	**0.498**	0.596	0.867	0.859	**0.705**
NUIST_NESM3*	0.120	0.478	0.868	0.644	0.527
SNU_SAM0-UNICON	0.226	**0.810**	0.759	0.662	0.614
ECMWF_ERA5	1.000	1.000	1.000	1.000	1.000
NASA_MERRA2	0.653	0.912	0.920	0.965	0.863

are found within 250 km of this location, the track is terminated.

5) We impose some additional constraints on candidate tracks to filter out heat lows and quasi-stationary troughs:
   - All tracks must have a duration of at least 48 h.
   - All tracks must have at least one point in a bounding box for the South Asian monsoon (70°–95°, 5°–32°N).
   - At least one point in the track must exceed an 850-hPa vorticity of 1×10^{-5} s^{-1}.
   - The average precipitation within 400 km of the LPS track must exceed 1 mm day^{-1}.
   - The distance between the track genesis and termination points must exceed 100 km.
   - Track genesis must be south of 25°N.

Each of these criteria are easily surpassed by all real LPSs (Hunt and Turner 2024). Versions of this algorithm have been used for monsoon LPSs by a number of authors (e.g., Martin et al. 2020; Dong et al. 2020; Roy and Rao 2022).

b. *FLIP score*

To evaluate the ability of CMIP6 models to simulate LPSs, we develop a multicomponent score, termed the frequency, location, intensity, and precipitation (FLIP) score. The FLIP score quantifies model performance across four key LPS characteristics and is computed over the historical period, relative to ERA5. The components are computed thus

1) Frequency. The total number of LPSs in each year is counted, giving a distribution for seasonal frequencies. This distribution is then compared with ERA5 using the Kolmogorov–Smirnov (K–S) statistic. The score ($1 - \mathrm{KS}^2$) measures how closely the model distribution of frequencies matches ERA5.
2) Location. Kernel density estimates of LPS track density for the whole period are computed, and maps of model values are regressed against ERA5; the score is the R^2 value.
3) Intensity. The maximum LPS intensity, i.e., the highest value of T63 spectrally truncated 850-hPa relative vorticity,

measured at the system center, is computed for each track. This distribution of peak intensities is then scored against the ERA5 benchmark using a K–S test, as for frequency. Use of the spectrally truncated vorticity makes this metric invariant to resolution over CMIP6 models.

4) Precipitation. Six-hourly precipitation is averaged within 400 km of the LPS center. This gives a precipitation time series for each LPS. All time points from each LPS are used to create a distribution of LPS precipitation, which is scored against ERA5 using a K–S test as in frequency and intensity.

The final FLIP score for a given model is the mean of the four component scores. We use the K–S test because it makes no prior assumptions about the underlying distributions (e.g., that they are Gaussian). In other words, it is nonparametric. Thus, we measure distributional fidelity using the K–S score and spatial fidelity using pattern correlation. For all three components, the best possible score is 1, indicating that the distributions are indistinguishable from ERA5, and the worst possible score is 0, indicating absolute certainty that the distributions are different. An advantage of this approach is that the component scores are constructed orthogonally. Therefore, for example, a model with 20% too many LPSs would have a poor frequency score, but the location score (despite the frequency bias being present in the track density estimate) would not be affected. Additional robustness checks, where we replaced the individual component scores with their cross-model z scores or quantiles, did not yield meaningful changes to the results. We use the overall FLIP score as a weighting term when computing multimodel means. The same FLIP score is used for all LPS characteristics, regardless of whether it has a corresponding FLIP component (e.g., intensity).

FLIP scores and their components are given for each model in Table 1.

c. Baselines and global warming levels

In this study, we will make considerable use of global warming levels (GWLs), a measure of how much global warming has occurred relative to some baseline. We define, for each model, a preindustrial reference temperature T_{ref} as the area-weighted ($\cos\phi$) global mean of annual near-surface air temperature (CMIP6 variable `tas`) averaged over 1850–1900. The GWL for year t is then the 30-yr trailing global-mean `tas` anomaly relative to this reference:

$$T_{\mathrm{ref}} = \frac{1}{N_{\mathrm{PI}}} \sum_{\tau=1850}^{1900} \langle T(\mathbf{x},\tau) \rangle_A,$$

$$\tilde{T}(t) = \frac{1}{30} \sum_{\tau=t-29}^{t} \langle T(\mathbf{x},\tau) \rangle_A,$$

$$\mathrm{GWL}(t) = \tilde{T}(t) - T_{\mathrm{ref}}.$$

Here, $\langle \cdot \rangle_A$ denotes the area-weighted global spatial mean. For years near and after 2015, the 30-yr window spans historical and SSP years as needed. Note that we use this backward-looking rolling mean to account for the diversity of trajectories that arise from the different SSPs from 2015 onward. A centered approach would mean having to choose an SSP when computing the GWL for a year near the end of the historical period. Note also that where we compare timelines of CMIP6-derived and reanalysis LPS statistics, we shift our benchmark period to 1995–2014, consistent with IPCC guidelines (Chen et al. 2021), as our reanalysis data are not available prior to 1940.

When computing LPS statistics for different GWLs, we ensure the statistics are robust by using a GWL window. This is fixed throughout the study at a width of 0.5°C. Thus, for example, when statistics are presented for a GWL of 2°C, we include all years with a GWL between 1.75° and 2.25°C.

In addition, we compute a "local" warming level that is over an approximate region affected by LPSs, 74°–92°E, 16°–26°N. This will allow us to more accurately compute the effect of warming on local thermodynamics, such as the Clausius–Clapeyron effect, recognizing that local warming—even over 30-yr means—may differ from global warming. We show the relationship between GWL and regional warming in Fig. 1. For a given GWL, the warming over India and the Bay of Bengal is typically about 0.25°C, reducing at higher GWLs. The difference is not significantly sensitive to scenario.

d. Storylines

Storylines (Shepherd et al. 2018) provide a framework for representing uncertainty in climate change projections by constructing physically self-consistent narratives that explain plausible but distinct future pathways without prescribing fixed probabilities. Instead of relying on probabilistic ensemble projections, i.e., the CMIP6 multimodel ensemble, storylines emphasize understanding the causal mechanisms—such as the interaction between changes in thermodynamics and circulation—that drive regional climate responses. In this study, we will use a storyline approach to investigate how diverse projections of changes to the monsoon circulation and moisture rectify onto LPS statistics, giving us two advantages: that the projected changes in LPS statistics become easier to explain, and that future decision-making is aided by attaching these changes to physically plausible pathways.

There are many ways to construct climate storylines (Baulenas et al. 2023; Baldissera Pacchetti et al. 2024). These are typically driver-conditioned, e.g., some important drivers of variability are identified with fields then regressed onto metrics of those drivers (Zappa and Shepherd 2017; Monerie et al. 2023). In our study, we do not want to presuppose those drivers and instead use an unsupervised clustering approach. This method provides a compact, physically self-consistent sampling of the CMIP6 uncertainty space, complementary to the driver-conditioned approach of the studies above, and are still interpretable a posteriori in terms of moisture availability and steering flow.

Our approach is described below.

1) The variables used for clustering are seasonal means (June–September) of 850 hPa u, v, and specific humidity. These

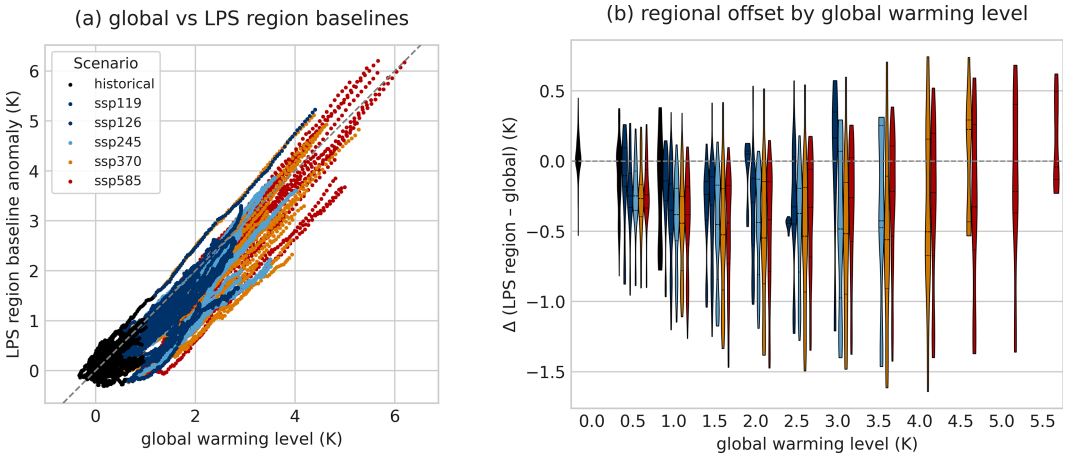

FIG. 1. The relationship between GWL and regional warming over India and the Bay of Bengal (i.e., the region affected by LPSs). (a) A scatterplot showing LPS regional warming against GWL for each model scenario year. The 1:1 line is given by gray dashes. (b) Violin plots showing the difference between the two as a function of scenario and GWL, subject to the requirement that at least 20 model scenario years of data are available. The LPS region is defined as 74°–92°E, 16°–26°N. Warming levels are computed as mean 2-m temperature over the previous 30 years against the respective 1850–1900 baseline. For GWL, these are annual means; for the regional warming, these are June–September means.

are taken for each model scenario year with GWLs of either 0° or 2°C. The choice of 2°C arises from policy relevance (it is a threshold value in the Paris agreement) and statistical robustness (there is good model coverage at this GWL, and the signal is likely stronger than internal variability).

2) The mean is computed for the 0°C values of each variable in each model (leaving the spatial dimensions intact). This is then subtracted from the respective 2°C scenario years for each model to give the difference relative to the baseline.
3) The variables for each model scenario year are interpolated onto a common 1° × 1° grid and standardized.
4) The model-scenario-years are concatenated along the time dimension. The spatial dimensions are flattened into a single dimension, and the variables are concatenated along this spatial dimension.
5) *k*-means clustering is applied to the dataset, with the elbow method used to determine the optimal number of clusters (four).
6) Information on LPS statistics is pulled through this pipeline in parallel, to allow for quick computation once the clusters have been assigned.

4. Results

a. Model evaluation

We start with an analysis of model LPS frequency and location, evaluated across the historical period (Fig. 2). These are compared against two reanalyses, shown in the bottom right of Fig. 2. We note that the difference in ERA5 and MERRA-2 track densities is not explained by the different dataset lengths (not shown). There is considerable variability in the track density between the CMIP6 models. Some closely resemble the reanalyses, such as the two HadGEM3 variants, and this is reflected in their high FLIP-location scores (0.82 and 0.88; see Table 1). Others deviate considerably, such as the two IPSL models, whose tracks are too far south, and AWI-ESM-1-1-LR, whose tracks are mostly confined to the western edge of the Bay of Bengal. These are reflected in low FLIP-location scores, all below 0.3. In general, there are two centers of action in the reanalyses: one at the head of the Bay of Bengal, and one inland, over central India. Only about half the CMIP6 models capture the latter.

Figure 2 also provides information on mean LPS frequency. Again, there is considerable variability among the models, with some considerably undersimulating LPS frequency (e.g., ACCESS-ESM1-5, whose FLIP-frequency score is 0.002) but many doing a reasonably good job. However, the FLIP-frequency score also takes into account the distribution arising from interannual variability, which most models significantly underestimate. The standard deviation in seasonal LPS frequency in ERA5 is 4.2, the CMIP6 multimodel mean (MMM) is only 3.5. As a result, the FLIP-frequency scores are low for most models.

Not shown in Fig. 2, but available in Table 1, are the FLIP-intensity and FLIP-precipitation scores. For both, most models score quite highly. On average, models slightly underestimate LPS intensity and precipitation but capture their respective interannual variability well. We show the FLIP scores against model resolution in Fig. 3. There is a significant negative correlation ($r = -0.66$) between model grid spacing and FLIP score, although this relationship is slightly weaker in the three pairs of models that differ only in resolution. The worst performing model is IPSL-CM5A2-INCA, which has very coarse resolution. However, some models with coarse resolution do actually perform quite well (e.g., GFDL-CM4). Similarly, almost all of the high-resolution models perform relatively well

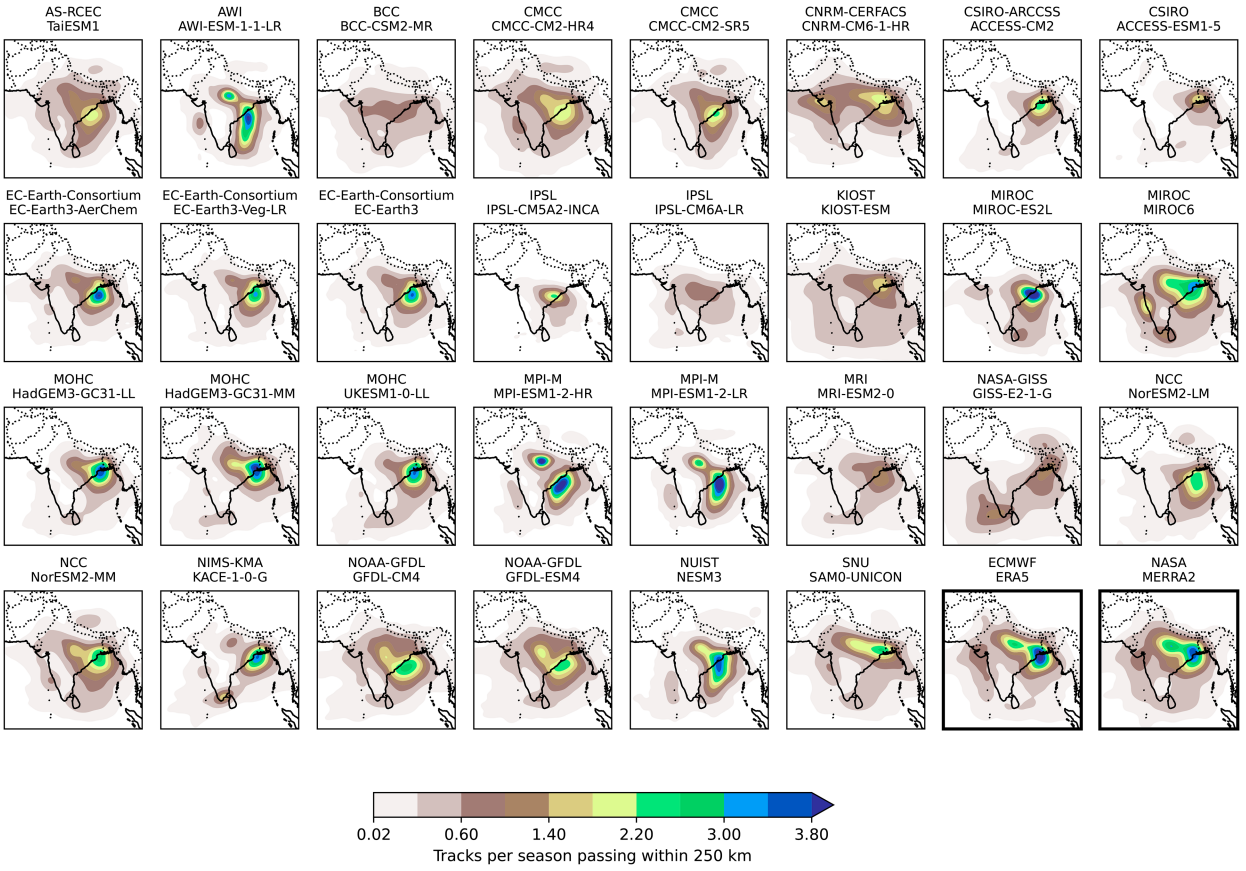

FIG. 2. Monsoon LPS track density in the historical run for available CMIP6 models (shown for 1940–2015). LPS tracks are converted to density using a Gaussian kernel density estimate and are shown as a seasonal average. In the bottom right, the mean track density for two reanalyses, ERA5 (1940–2015) and MERRA-2 (1980–2015), are shown for comparison, using as many available overlapping years as possible.

(e.g., CMCC-CM2-HR4, CNRM-CM6-1-HR) with the notable exception of BCC-CSM2-MR which scores poorly across all FLIP components.

b. Trends by global warming level

Having assessed model performance at simulating LPS populations in the historical period, we now assess how LPS behavior might change in future climate scenarios. We remind the reader that all multimodel means (but not, e.g., interquartile ranges) are hereafter weighted using the model FLIP scores. We start by looking at trends in a selection of LPS characteristics over the historical and future periods, using a range of SSP scenarios (Fig. 4).

There is a significant increase in projected LPS frequency (Fig. 4a) that starts in the historical period around the 1990s and persists in all SSPs through to the end of the twenty-first century. Higher SSPs tend to have a greater increase than lower SSPs. Despite pronounced internal variability, almost all realizations report more LPSs at the end of the twenty-first century than at the end of the twentieth. The inflection point toward the end of the twentieth century is consistent with earlier studies that demonstrated the change in dominance from aerosol forcing to greenhouse gas (GHG) forcing which occurred around this time (Lau and Kim 2017).

There is a significant decline in LPS intensity (Fig. 4a) throughout the twenty-first century in all SSPs except SSP126, which exhibits an initial decline during the first half of the century before returning to within the 1995–2014 historical baseline. As with frequency, the magnitude of these trends scales well with SSP; however, the decline does not emerge during the historical period, during which LPS intensity is reasonably constant. This decline in intensity is consistent with previous studies (Sandeep et al. 2018; Vishnu et al. 2023). Combined with the increasing frequency, we deduce that future monsoons are likely to have far more weak LPSs than the present day. The future of strong LPSs (i.e., monsoon depressions) requires further analysis that follows later.

There is a significant increase in per-LPS precipitation, i.e., rainfall occurring within 400 km of the LPS center (Fig. 4c). As with LPS frequency, this trend seems to emerge in the 1990s, i.e., in the historical period, continuing in each of the SSPs through to the end of the twenty-first century. The trend in all SSPs is much larger than the interannual variability, and more so than for frequency or intensity. This is to the extent that in SSP126, while LPS intensity and frequency recover to

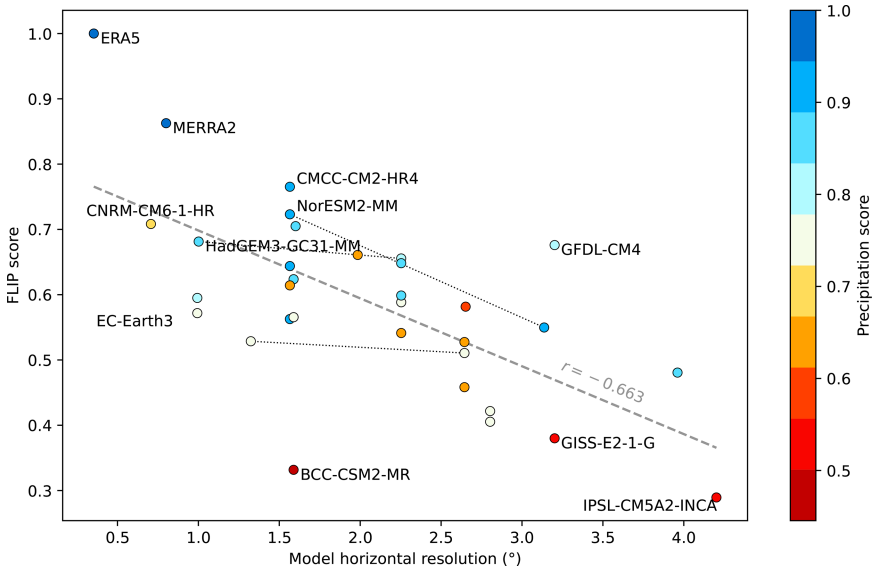

FIG. 3. Model FLIP score as a function of horizontal resolution, evaluated over the historical period (1850–2015). The FLIP score combines information on the differences between modeled and observed distributions in LPS frequency, intensity, location, and precipitation to estimate the skill of individual models in simulating realistic LPSs. Individual models are colored by their precipitation score. Horizontal resolution is taken as the hypotenuse of the mean longitude and latitude spacings. The best-fit line (not including the reanalyses) and correlation coefficient are shown in gray. Dotted black lines connect the three pairs of models that differ *only* in their resolution, e.g., HadGEM3-GC31-LL and HadGEM3-GC31-MM.

near-baseline values by the end of the century, this is not true of LPS precipitation. Coupled with the significant increase in LPS frequency, it is clear that the total LPS-associated rainfall per season will also increase with global warming.

There is no significant trend in the mean LPS post-landfall duration (Fig. 4d), and we note that this particular characteristic is subject to substantial interannual and interdecadal variability, implying a relationship with slowly varying modes of variability such as ENSO or the Pacific decadal variability (PDV), although it is beyond the scope of this study to explore these relationships. For the fraction of LPSs making landfall (Fig. 4e), there is a significant increasing trend only in the two warmest SSPs (370 and 585). The multimodel means for SSP126 and SSP245 return to baseline levels by the end of the twenty-first century. There are, however, significant increases in projected LPS propagation speed (Fig. 4f) in all SSPs, despite pronounced interannual variability. There is also an increasing trend in interannual variability.

While this approach is informative, different models warm at different rates due to their range of sensitivities and so extracting values, e.g., for a given year, may lead to ambiguous interpretation. Instead, we now separate according to global warming level (Fig. 5), measured relative to a preindustrial baseline. This is helpful, as much importance is given to the difference in impacts between 1.5° and 2°C of global warming (Masson-Delmotte et al. 2018).

Many of the same trends emerge: relative to the 0°C baseline, both 1.5° and 2°C GWLs exhibit significant increases in LPS frequency, precipitation, landfall fraction, and propagation speed, and a significant decrease in LPS intensity. Significance here is ascertained using a Kolmogorov–Smirnov test. Post-landfall duration also increases with GWL, but the difference against the baseline is only statistically significant at higher levels (2.5° and 3°C). Interestingly, neither LPS frequency nor intensity changes significantly between 1.5° and 2°C, but post-landfall duration and mean propagation speed all increase significantly. This implies a step change in the number of systems penetrating more deeply into India, and therefore in the impacts felt over central and west India. We shall explore this more toward the end of the study. The unusual behavior of some statistics at 3°C, namely, a slight decrease from 2.5°C rather than the expected increase, as in Figs. 5d–f is probably due to reduced sample size. Even at SSP585, reaching a 30-yr mean GWL of 3°C only occurs toward the end of the twenty-first century.

A third way of visualizing these data is to separate GWLs by SSPs, as we do in Fig. 6. For the sake of brevity, we restrict this analysis to the first three statistics from the earlier analysis: LPS frequency, intensity, and precipitation. The leftmost column of Fig. 6 shows the CMIP6 multimodel ensemble, with thick lines denoting the multimodel means. For LPS frequency (top left subfigure), we see that while frequency increases with GWL for all SSPs, as expected, it increases faster in the weaker SSPs. For example, at 2°C, the projected change in the SSP585 pathway is 12% and in SSP126 is 18%. This difference increases further at higher GWLs: at 3°C, the projected change in SSP585 is 18% and in SSP245 is 32%. This suggests an important role for transient warming. The same is

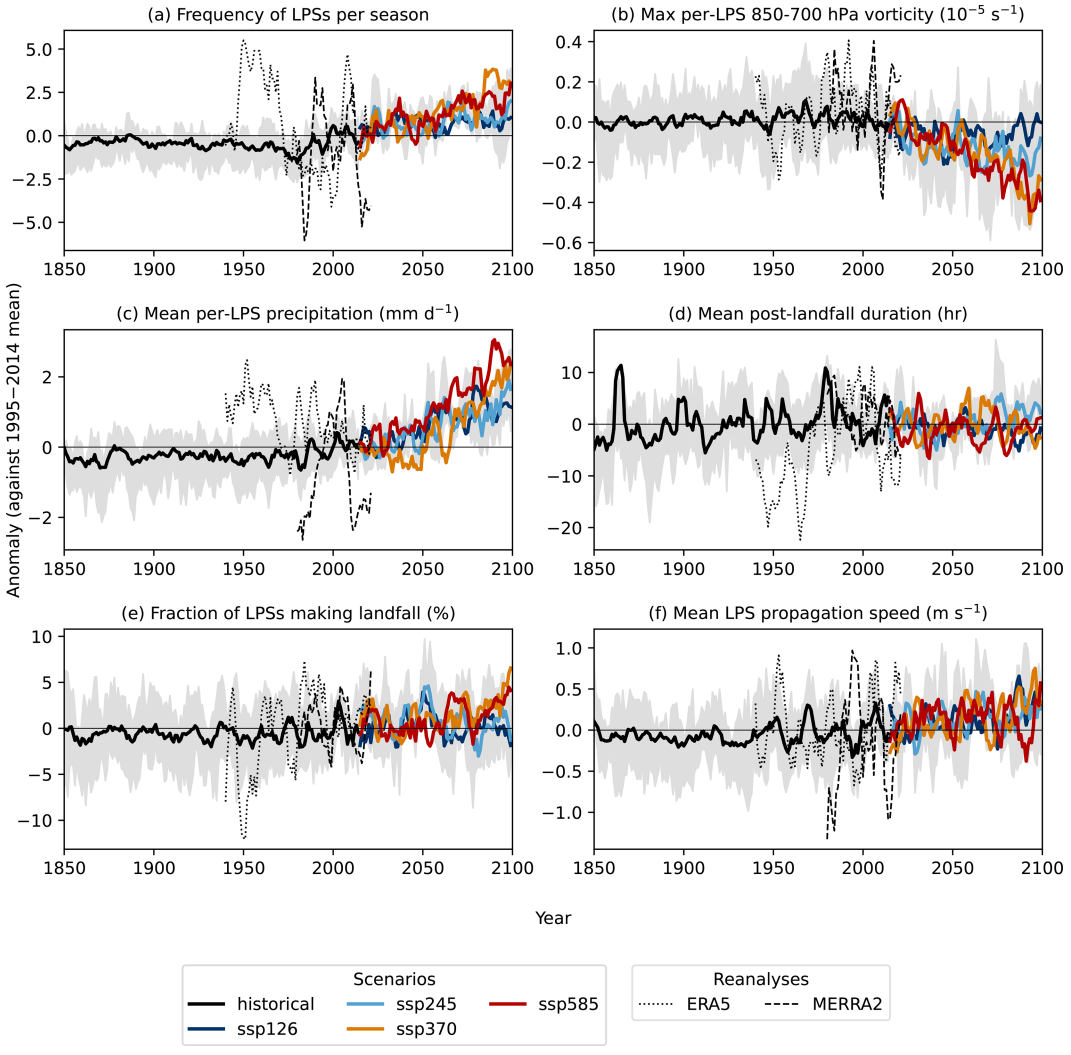

FIG. 4. Multimodel mean trends in LPS statistics across different CMIP6 scenarios, compared against a 1995–2014 historical baseline. For each monsoon season, we show (a) the total number of unique LPSs; (b) the average peak intensity of LPSs, measured using 850-hPa relative vorticity at the system center; (c) the mean precipitation falling within 400 km of each LPS; (d) the mean time between an LPS making landfall and dissipating, or for LPSs that spin up over land, their total duration; (e) the fraction of LPSs whose genesis is over the ocean but make landfall during their lifetime; and (f) the mean LPS propagation speed, computed across all track points. All values are smoothed using a 5-yr running mean. The gray shading indicates the model interquartile range for the historical scenario (before 2015) and the SSP245 scenario (after 2015). Dotted and dashed lines show the same statistic for reanalyses.

not, however, true for LPS intensity (middle row) or precipitation (bottom row), where the difference between SSPs is not significant. It is notable that, for precipitation, SSP126 scales at a lower rate than other scenarios. SSP1 relies on strong global air quality policies, including over India, and so has fewer aerosol emissions from South Asia than other scenarios for a given point in the near future (Samset et al. 2019). It is therefore possible that strong reductions in aerosol emissions over India in the coming decades may act to reduce the effect of global warming on increasing per-LPS precipitation.

Overall, internal variability is extremely low, as shown by the two large ensembles (MIROC6, central column; and MPI-ESM, right column). These have very little spread arising from their members—in some cases with individual members not visibly distinct from the ensemble mean (though noting our earlier caveat that we have a small sample size). Indeed, for each of the three parameters, the two LEs lie within the envelope of CMIP6. For example, for intensity, the CMIP6 MMM projects a decline of about 10% at a GWL of 4°C. Even though the MIROC6 LE projects a weak increase, there are still some CMIP members consistent with this. In conclusion, the CMIP6 column (left) indicates that, while there is a clear scaling of the response for each diagnostic with GWL, there is also a great deal of model—i.e., structural—uncertainty.

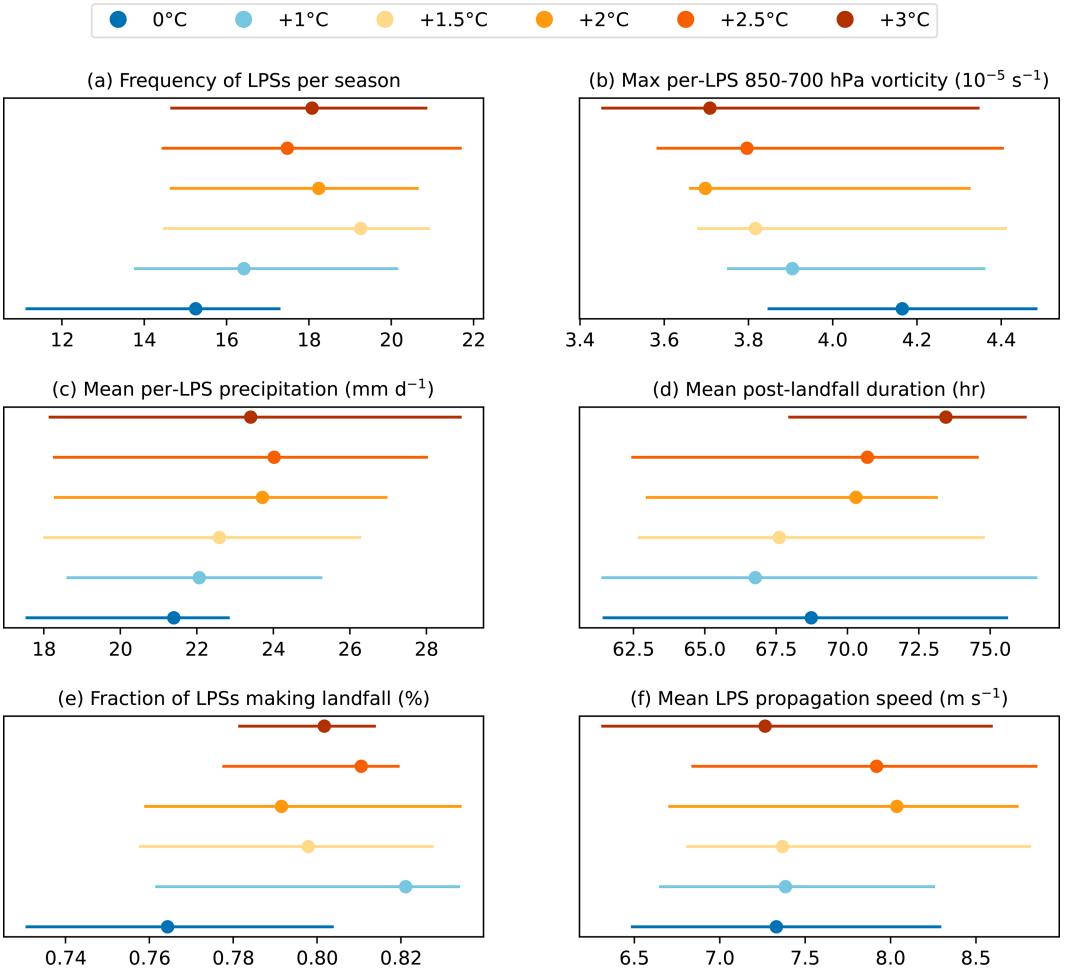

FIG. 5. Multimodel LPS statistics as a function of GWL. The same statistics as in Fig. 4 are used, except no baseline is subtracted. The circles indicate the multimodel mean, with the bars indicating the interquartile range of model means. In each case, all available scenarios are included, and a window width of 0.5°C is used, e.g., the 1.5°C contains any model scenario year in which the GWL was between 1.25° and 1.75°C. GWLs are computed relative to the preindustrial baseline for the model.

Finally in this section on LPS statistics, we turn to the covariability of LPS intensity and precipitation. In the present climate, LPS intensity and precipitation have a strong positive correlation (Hunt and Fletcher 2019) due to the importance of moist convective processes in LPS intensification (Diaz and Boos 2019) and the stronger moisture convergence offered by larger low-level wind speeds (Hunt and Turner 2022). However, as we have seen, LPS intensity is projected to decrease with global warming, while LPS precipitation is projected to increase. This in itself is not paradoxical—LPS intensity is ultimately constrained by dynamical processes (e.g., through barotropic instability arising from meridional gradients in zonal wind speed), whereas LPS precipitation is ultimately constrained by thermodynamic processes (i.e., moisture availability through Clausius–Clapeyron scaling). Even so, given their relationship with each other, further investigation is warranted.

Therefore, in Fig. 7, at each GWL, we separate LPSs into pentiles according to their peak intensity and plot the mean peak intensity against mean LPS precipitation. That gives us a trace across GWLs for each pentile, from the weakest lows to the strongest depressions. The multimodel mean is shown in Fig. 7a. In each intensity pentile, increasing GWL leads to monotonically increasing precipitation, but the effect scales differently in each pentile. In the weakest intensity pentile, mean LPS precipitation rises from 15.9 mm day^{-1} at a GWL of 0°C to 16.7 mm day^{-1} at a GWL of 3°C, an increase of 5% (considerably subC-C). In the strongest intensity percentile, mean LPS precipitation rises from 27.7 mm day^{-1} at a GWL of 0°C to 35.4 mm day^{-1} at a GWL of 3°C, an increase of 28% (superC-C). The interpretation of the results with respect to Clausius–Clapeyron scaling does not change if we separate by local seasonal warming instead of GWL (see Fig. 1).

We also see that the change in intensity with GWL differs across the pentiles. In the weakest intensity pentile, the mean peak LPS intensity falls from 1.63 to 1.43 $\times$ 10^{-5} s^{-1} as we move from 0° to 3°C, a drop of 14%. In the strongest

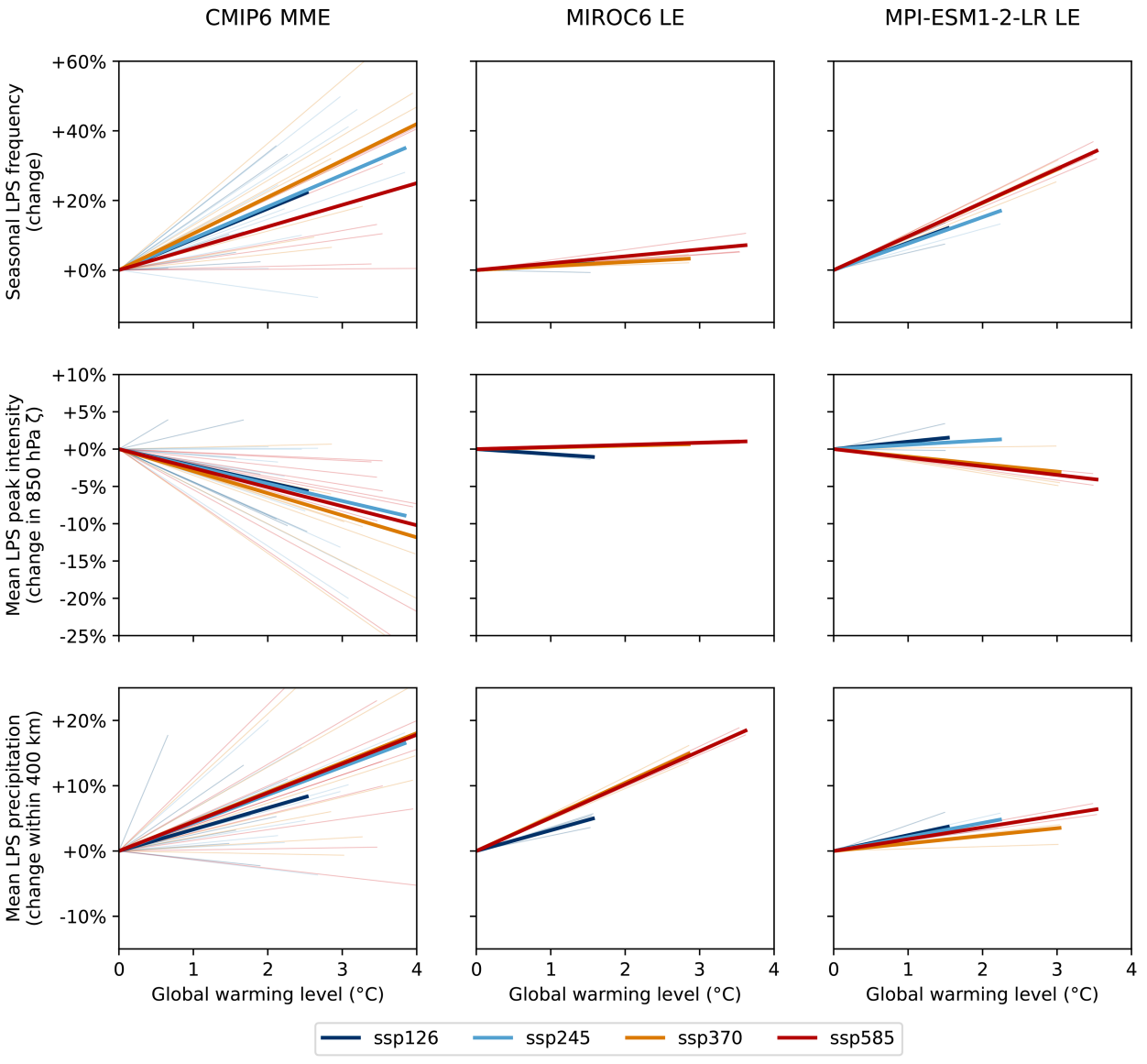

FIG. 6. Relationship between selected LPS statistics and GWL, as a function of SSP. (top) Number of LPSs per season; (middle) the average peak intensity of LPSs; (bottom) the mean precipitation within 400 km of LPS centers. These are shown for (left) the CMIP6 multimodel mean, (center) the MIROC6 large ensemble, and (right) the MPI-ESM-2-LR large ensemble. Results are shown as a best-fit line through all relevant model scenario year points. All values are shown relative to a 0°C historical baseline, computed for each model. Thin lines show individual models (for the MMM) or ensemble members (for the two LEs). Thick lines show the (left) MMM or (center and right) ensemble mean. SSP245 was not available for MIROC6LE.

intensity pentile, the drop for the same GWLs is from 6.93 to 6.87, or about 1%. In other words, mean precipitation increases with GWL, but this change increases at higher intensities.

These two patterns are present in two individual models with high FLIP scores (Figs. 7b,c), albeit with more noise present, with both projecting larger increases in LPS precipitation and reduced weakening (or even strengthening) for more intense systems. For the selected model with a poor FLIP score, NUIST NESM3, there is no coherent change in precipitation or intensity with GWL for any pentile.

Previous studies suggest that the driving mechanisms behind LPS intensity seem to be the same regardless of the strength of the LPS (Hunt and Turner 2024), and there is no reason to expect that to change with global warming. Therefore, changes in peak intensity are likely to continue to be driven by changes in barotropic instability. This is projected to fall in the Bay of Bengal, the main LPS genesis, and intensification region (Vishnu et al. 2023). Combined with the fact that precipitation scaling is sensitive to intensity, it is therefore likely that some kind of nonlinear positive feedback is at play. Increased moisture availability results in more precipitation,

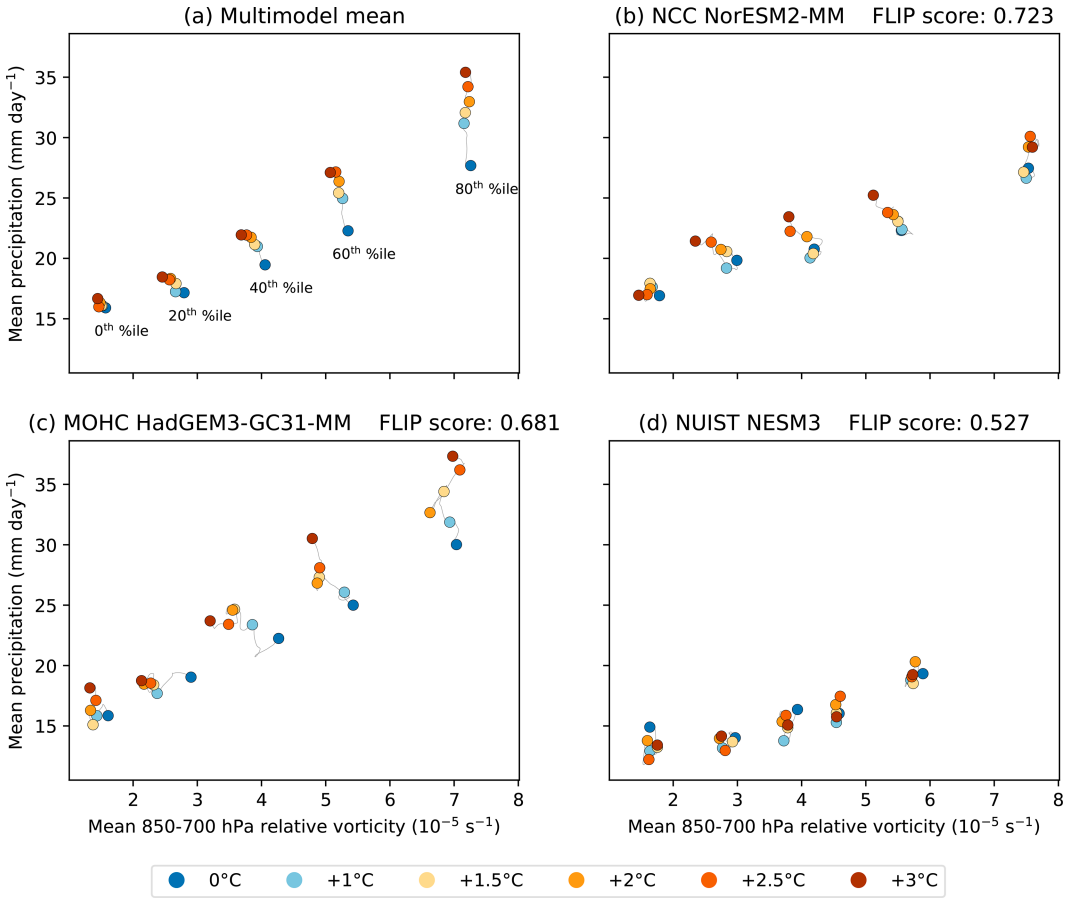

FIG. 7. Relationship between changing LPS intensity and precipitation as a function of GWL and LPS category. For each GWL, LPSs are separated into five pentiles based on their peak intensity, then mean LPS precipitation is plotted against mean peak intensity. (b),(c) Two models with high FLIP scores, (d) alongside a model with a poor FLIP score, and (a) the weighted mean across all models. The "20th percentile" refers to all LPSs with a peak intensity between the 20th and 40th percentiles.

and hence more convective vortex stretching and latent heat release. This allows LPSs to offset some of the climate-induced weakening and scales such that the most intense LPSs are able to offset it altogether. We will now explore possible reasons for this nonlinearity.

c. *Changes in LPS structure*

To understand some of the changes discussed in the previous section, we now turn to the composite structure of LPSs and how it is projected to change with global warming. We start with precipitation (Fig. 8). Compared to ERA5, the CMIP6 MMM at 0°C slightly underestimates precipitation. At the center, this underestimation is about 20%. This is also true for the modern CMIP6 baseline. This is a known bias in CMIP-class models (Sperber et al. 2013; Ashfaq et al. 2017). Similarly, there is a slight bias in the location of maximum precipitation relative to the LPS center, which is slightly to the southwest in ERA5 (as predicted by theory) but slightly to the northwest in CMIP6. Regardless, the spatial structure and magnitude of precipitation are sufficiently similar between ERA5 and CMIP6 that we can be relatively confident in the CMIP6 projections.

The projected change in LPS precipitation scales approximately linearly with GWL, as we expect from our earlier results in Figs. 5 and 7. At the LPS center, where the heaviest precipitation falls, the scaling is consistently superC-C (and is more so if we replace GWL with local warming level). This effect is strongest at 1°C, where we would expect uniform scaling of 7%; it in fact exceeds 14% just to the southwest of the center. At 3°C, the heaviest rainfall is scaled by slightly more than the expected C-C value of 21% but exceeds 28% in the lighter rain region further to the southwest. However, at each GWL, large areas of the composite have subC-C scaling, leading to the relatively weak scaling in the statistics presented earlier.

There are thus three common features across the GWLs: 1) superC-C scaling of maximum LPS precipitation; 2) subC-C scaling of precipitation in most of the LPS environment, especially to the north and east; and 3) the strongest scaling occurs several hundred kilometers to the southwest of the LPS center. This also implies a superC-C scaling of extreme rainfall associated with LPSs in a future climate, in agreement with

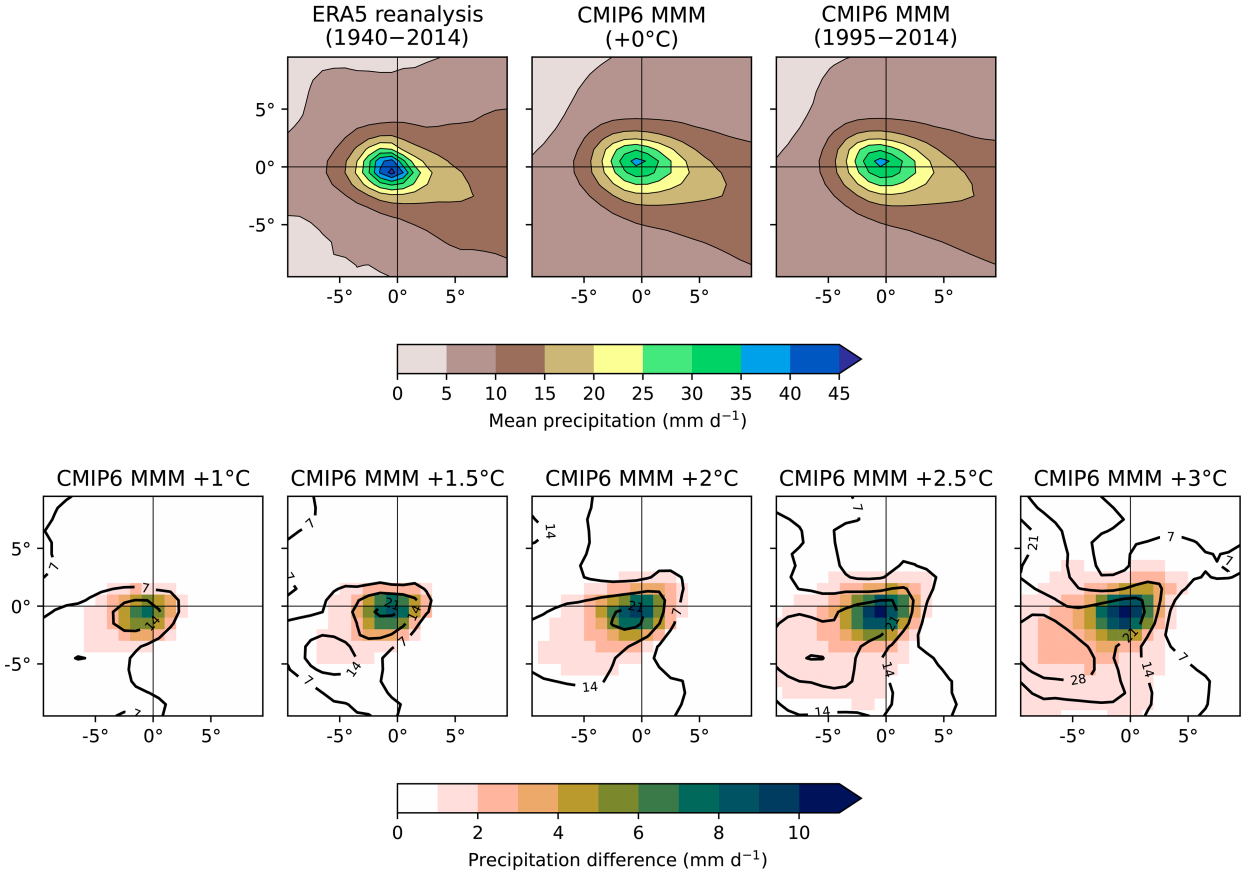

FIG. 8. System-centered composite footprints of LPS precipitation. (top) ERA5 [(left) 1940–2015)] and two model baselines [(center) a GWL of 0°C and (right) a modern baseline of 1995–2014]. (bottom) The composites for CMIP6 MMM at different GWLs, relative to the MMM 0°C baseline. Filled contours on the top row show absolute precipitation, colors on the bottom row show absolute precipitation differences, and line contours on the bottom row show the fractional increase as a percentage. Intervals of 7% are chosen to indicate sub or super Clausius–Clapeyron scaling. These composites are not rotated.

earlier studies (e.g., Vishnu et al. 2023). The statements in this paragraph do not change if we replace GWL with local warming level.

This superC-C scaling, both at the LPS center and more strongly to the southwest, cannot occur without some coupled feedback between the moisture and dynamics. However, we have already shown that LPSs tend to weaken with global warming (Fig. 5) and that the precipitation scaling happens regardless (Fig. 7). The scaling must therefore arise either from changes to the LPS structure—which we explore next—or the monsoon environment at large—which we explore in section 4d.

We now look at how the vertical structure of LPSs changes with global warming, using vertical-zonal cross sections of meridional wind speed (Fig. 9). As before, the top row compares composites from the CMIP6 MMM at a GWL of 0° and ERA5. The vertical structure of the LPS in the MMM is very well represented, with both the magnitude (peak winds speeds around 7 m s^{-1}) and asymmetrical structure appearing similar to ERA5. The asymmetrical structure arises as, for a typical LPS, much of its western flank is over land—with high friction reducing wind speeds below 850 hPa—whereas most of the eastern flank is over the ocean, with much surface friction.

As expected from the projected fall in LPS intensity, increasing GWL reduces the wind speeds around the LPS (bottom row of Fig. 9). However, this reduction in intensity does not scale equally across the composite LPS. In particular, near the boundary layer (i.e., at pressures above 800 hPa), the winds weaken far less than they do in the free troposphere (e.g., at 700 hPa), even over the ocean. For example, at a GWL of 2.5°C, the winds at 500-km radius on the western flank of the composite LPS weaken by about 0.6 m s^{-1} but only about 0.05 m s^{-1} at 925 hPa. This means that while LPS intensity falls with GWL, the near-surface winds remain relatively constant. Thus, for a given LPS intensity, near-surface winds actually increase with GWL, driving increased frictional moisture convergence and hence increased precipitation. However, this does not explain the superC-C scaling we saw in Fig. 8, for which we will shortly turn to the monsoon environment.

Aside from the different scaling across pressure levels, we also note that the radius of maximum wind speed is projected

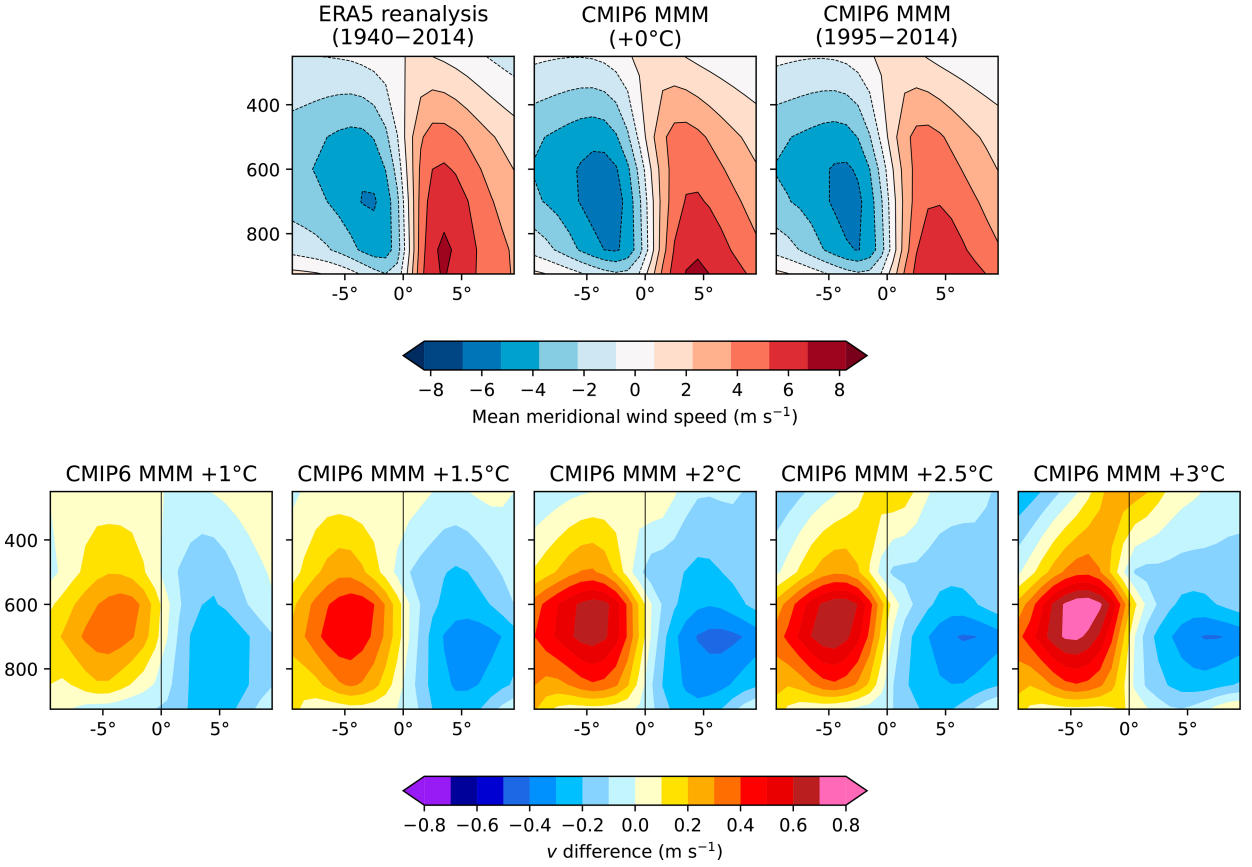

FIG. 9. System-centered vertical-zonal cross sections of meridional wind speed. (top) ERA5 [(left) 1940–2015)] and two model baselines [(center) a GWL of 0°C and (right) a modern baseline of 1995–2014]. (bottom) The composites for CMIP6 MMM at different GWLs, relative to the MMM 0°C baseline. Filled contours on the top row show the mean wind speed (positive values indicating southerlies), colors on the bottom row show the differences.

to change, too. The largest reductions in 700-hPa wind speed occur at a radius of about 5°, further from the center than the maximum wind speeds at 0°, which are around 3° from the center. This implies a shrinking of LPS circulation with GWL, with the radius of maximum wind speed moving closer to the center.

d. *Monsoon storylines*

We now turn to the effect of global warming on the large-scale monsoon environment to explain some of the projected changes in LPSs discussed earlier. We start with a simple trend analysis, regressing lower-tropospheric humidity and winds against global warming level (Fig. 10). The trend in specific humidity increases with latitude over India (Fig. 10a), resulting in a stronger meridional gradient in 850-hPa specific humidity with increasing global warming level. This has two important implications. First, northerly winds to the west of the vortex will advect this moisture downgradient, further increasing precipitation ahead (i.e., to the west) of the LPS. The reverse is true behind (i.e., to the east) of the LPS, where southerly winds advect relatively dry air toward the rear flank, reducing precipitation. This effect explains the pattern we saw in Fig. 8, with superC-C scaling to the west of the LPS center and subC-C scaling to the east. Due to quasigeostrophic balance in an environment of strong easterly wind shear, the heaviest precipitation associated with an LPS occurs to the southwest of its center (Rajamani and Rao 1981). Therefore, a positive meridional gradient in humidity serves to increase this maximum, in turn increasing the average LPS precipitation.

The second implication is for moisture-vortex instability, which argues that LPS intensification arises predominantly from positive meridional advection ahead of the LPS. We compute the linearized change $\Delta(-v\partial_y q) \approx -(\overline{v}_{\mathrm{LPS}}\partial_y q' + v'_{\mathrm{LPS}}\partial_y \overline{q})$. The first term on the right-hand side measures the change in meridional moisture advection from the increase in background moisture gradient; the second measures the change in advection from weakening LPS circulation. The v_{LPS} is taken at 850 hPa from the cross sections used to make our LPS-centered composites (Fig. 9), averaged between 100 and 600 km to the west of the LPS center. The $\partial_y q$ is taken from the background (Fig. 10b).

Over the Bay of Bengal, the baseline advection is 0.26 g kg^{-1} day^{-1} and increases by 0.01 g kg^{-1} day^{-1} K^{-1} (3.6% K^{-1}; 7.2% at +2°C). The gradient term contributes *sim*6.6% K^{-1} (13% at +2°C), while the circulation term contributes ~−3.0% K^{-1} (6.0% at +2°C). Thus, the increase in meridional moisture gradient wins because the weakening of

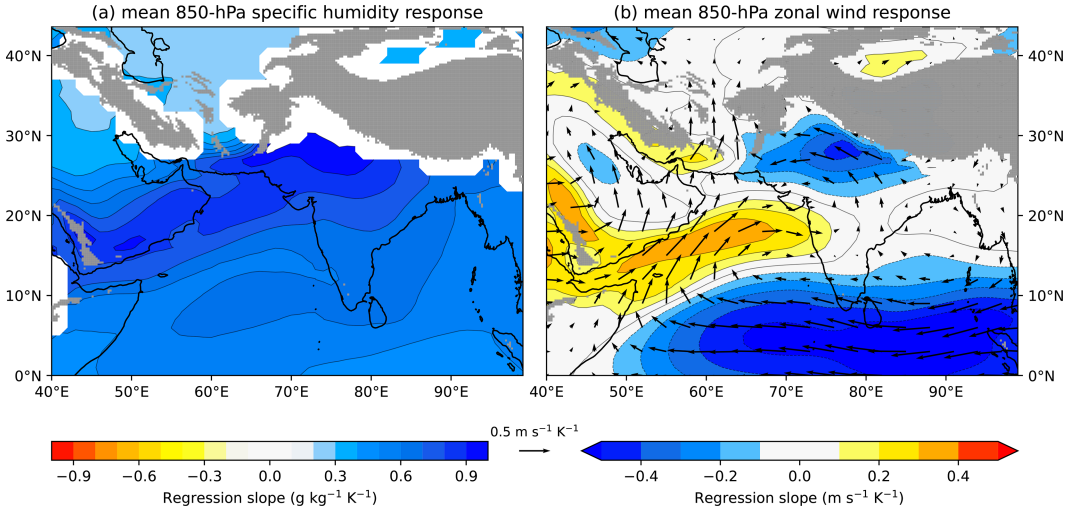

FIG. 10. Sensitivity of monsoon humidity and winds to global warming. For each model, a pointwise linear regression is computed between seasonal means (June–September) of the variable of interest and GWL (computed using 30-yr annual means). The figure shows the CMIP6 multimodel mean of the regression slopes. (left) The 850-hPa specific humidity; (right) 850-hPa winds, with vectors showing both u and v components, but the colors showing the zonal wind response only. Gray masking indicates where orography causes the mean surface pressure to fall below 850 hPa.

LPS circulation only partially offsets the increase. Over central India, the baseline advection is small (0.02 g kg^{-1} day^{-1}). The absolute change is +0.07 g kg^{-1} day^{-1} K^{-1} (~+0.14 at +2°C), of which the gradient term accounts for 101% (whereas the change from circulation is only ~−1%). This would certainly support deeper inland penetration of LPSs in a warmer climate. We might also expect an increase in LPS intensity in response to the strong trend in moisture gradient; however, as we have seen, this is not the case and so other factors must clearly play a role.

One possible such factor is the low-level circulation itself (Fig. 10b). Continued global warming is projected to weaken the lower-tropospheric summer monsoon circulation (Ashrit et al. 2003; May 2004; Doblas-Reyes et al. 2021), consistent with the pattern presented here—weaker westerlies over the Arabian Sea and southern and central India and weaker easterlies over northern India, consistent with the changes reported in Fig. 4b of Vishnu et al. (2023). There is also a projected change to the mean monsoon circulation. In particular, the Somali jet—which becomes the monsoon westerlies—becomes more aligned to the northeast, while the monsoon trough extends to the west and moves slightly northward. These are break-like phenomena and would lead to increased monsoon precipitation over the western and northwestern states of India, such as Gujarat. This is consistent with recent observations showing mean monsoon rainfall has increased in these regions (Prabhu and Chitale 2024). There are thus two implications for LPSs. First, drawing on moist barotropic theory, which has been proposed to explain their intensification rate (Diaz and Boos 2019) or at least their peak intensity (Hunt and Turner 2024), we note that the meridional gradient in lower-tropospheric zonal wind speed decreases slightly over the Bay of Bengal but increases considerably over western India. In other words, the large-scale instability from which LPSs grow is reduced over their genesis region but increased over their lysis region. This changing circulation pattern may therefore explain the projected trends toward weaker but longer-lived LPSs that we discussed earlier. We would also expect deeper inland penetration of LPSs, as the environment becomes more hospitable over western India. We will explore this toward the end of the paper.

As earlier studies have shown, projected trends in monsoon circulation shown in the MMM aggregate several possible dynamical futures (Bhave et al. 2018; Dessai et al. 2018). These diverse but self-consistent futures and analysis of their impacts are often referred to as dynamical "storylines" (Shepherd et al. 2018), and they provide a way to represent future climate uncertainty. We now examine different monsoon storylines and their impacts on LPSs (Fig. 11). Four clusters, computed using seasonal means of 850-hPa u, v, and specific humidity across all available models at a GWL of 2°C, show four distinct storylines. As in Bhave et al. (2018) and Dessai et al. (2018), they are largely distinguishable by the changes to the moist westerlies along the west coast.

Cluster 1 is the least common and represents the most extreme response—substantial moistening of the lower troposphere over the entire domain as well as considerable changes to the circulation. These changes include a redirection of the monsoon westerlies toward the northwest of India and an anomalous anticyclone over the Bay of Bengal. Not surprisingly, given the large increase in available moisture, this cluster also leads to the largest increase in per-LPS precipitation, at nearly 17%. In contrast, the considerable weakening of the monsoon trough over the Bay of Bengal, along with the associated fall in barotropic instability, results in a projected decrease in LPS intensity of 20%, also the largest of the four clusters.

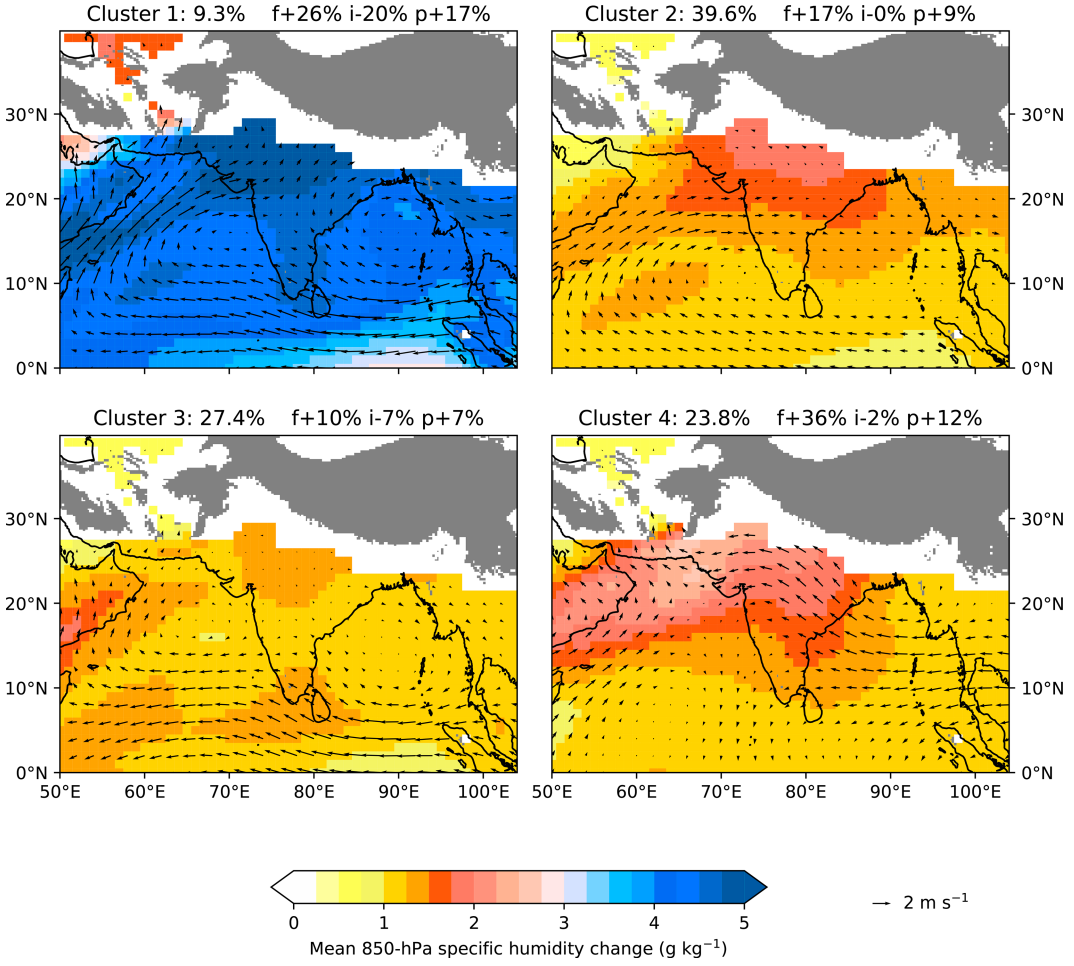

FIG. 11. Storylines for the summer monsoon at a GWL of 2°C. For all models and scenarios with monthly mean data, seasonal averages of 850-hPa specific humidity, u and v are taken for all years, where the 30-yr running mean of GWL is between 1.75° and 2.25°C. From these, the 0°C model baseline is subtracted. The model scenario years are then concatenated in time and clustered across all three variables simultaneously using k-means. The four panels show the composite means of anomalous specific humidity and wind for each of four clusters derived using this method. The subfigure titles indicate the cluster number, the number of samples in each cluster expressed as a percentage of the total, and then LPS statistics for each cluster. The respective LPS statistics are frequency, mean peak intensity, and precipitation, each expressed as the cluster mean relative to the 0°C baseline of the respective models.

Cluster 2 is the most common and reflects a general strengthening of the monsoon westerlies along with some extension of the monsoon trough toward the northwest of India. In this storyline, there is almost no change to the circulation over the Bay of Bengal or north India, and as such LPS intensity remains fairly constant. The 850-hPa specific humidity increases everywhere, with the largest increase over north India, increasing the meridional gradient as we saw in Fig. 10. Cluster 3 is also quite common and has the smallest changes of any of the storylines. Over India, there is a slight but fairly uniform increase in specific humidity and very weak adjustment to the circulation.

Consistent among clusters 1–3 is the presence of stronger off-equatorial easterlies. These are absent in cluster 4, whose projected circulation change is considerably different. Here, there are enhanced moist southwesterlies impacting Gujarat and Pakistan, as well as stronger easterlies across the whole of north India. This leads to increased moisture convergence over north and west India and hence a significant increase in the mean specific humidity over that region. This moistening leads to a greater increase in per-LPS precipitation (12%) than we saw in clusters 2 and 3. However, of particular interest in cluster 4 is the projected change in LPS frequency, which at 36% is far higher than the other three clusters. We speculate that this arises from the anomalous easterlies over the Bay of Bengal and Southeast Asia. Between 30% and 60% of LPSs spin up from precursor vortices that can be tracked from origins over Southeast Asia, the South China Sea, or the west Pacific (Saha et al. 1981; Chen and Weng 1999; Meera et al. 2019), and regional climate models fed with climatological boundary conditions hugely underestimate LPS frequency (Levine and Martin 2018). We therefore propose

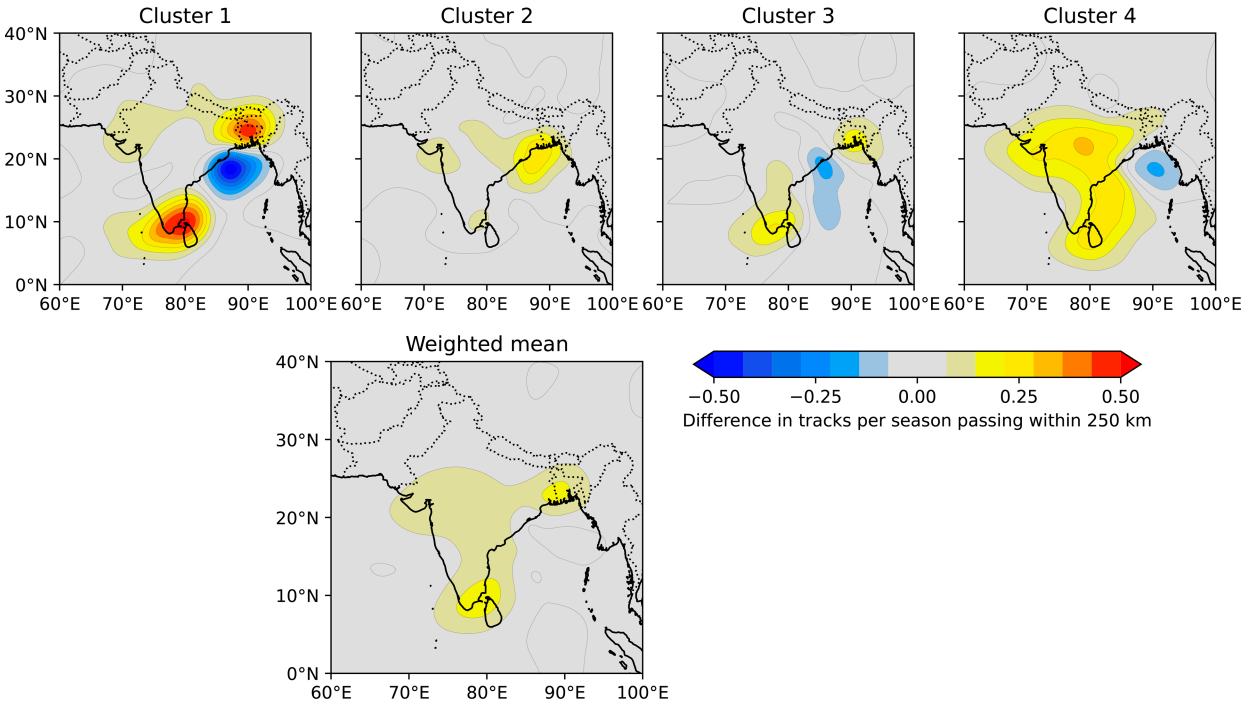

FIG. 12. Changes in seasonal-mean LPS track density for each of the 2°C storyline clusters in Fig. 11. These are multimodel means expressed as changes relative to the respective 0°C model baselines. As in Fig. 2, densities are computed using a Gaussian kernel density estimate and expressed as the number of unique LPS tracks passing within 250 km of a given point per season. (bottom) The mean across the four clusters, weighted by their frequency (see Fig. 11).

that these stronger easterlies create an environment more conducive for precursor vortices to reach the Bay of Bengal, where they can subsequently spin up into LPSs. These beneficial conditions are absent in the other three clusters, which consequently have smaller gains in LPS frequency.

While all clusters show an increase in LPS frequency, it is clear from their diverse circulation changes that the changes to track density will not be homogeneous. To investigate, we composite track density estimates for each of the four clusters in Fig. 12. Cluster 1 was associated with an anticyclonic anomaly over the Bay of Bengal. This is detrimental for LPS growth as it decreases barotropic instability and cyclonic shear, which is reflected in a large decrease in track density over that region. These tracks seem to migrate to the north and south, where local cyclonic shear is increased, resulting in significant increases in track density over Bangladesh, south India, and Sri Lanka. Note that the higher moisture availability and increase in cyclonic shear over the Arabian Sea do not seem to be converted to increased LPS track density over that region, with only a slight gain over Gujarat. This may be due to an absence of precursor vortices over that region, as in the present day (Deoras et al. 2021).

Cluster 2 represents, more or less, a strengthening of the present-day lower-tropospheric monsoon circulation. The projected LPS track density adjusts accordingly, increasing in frequency most in the regions they currently impact (the Bay of Bengal and east India). There is also a small increase over west India. However, the strengthening of the monsoon trough and increased moisture availability allow a much deeper penetration of some LPSs inland, with the result that track density increases considerably over central peninsular India. In contrast, cluster 3 showed very weak lower-tropospheric circulation changes over India, and this is reflected in very little change to LPS track density—except over Bangladesh and Sri Lanka (as in cluster 1), where increased moisture availability may play a role.

Cluster 4 is of particular interest, as this had strong anomalous easterlies over Southeast Asia propagating across the whole subcontinent, which we speculated led to increased transmission of upstream LPS precursors. In fact, not only is LPS frequency significantly increased, but so is their inland penetration, with many more tracks reaching central, west, and northwest India. There is thus a potentially serious impact over west and northwest India. As climate change enables LPSs to reach this region, which is very rare in the present day, they are met with much greater moisture availability.

The net effect, averaged over the four storylines, is for more monsoon LPSs overall, but also a growing region of impact—we expect to see more systems impacting regions that are typically not commonly affected by present-day LPSs, such as Sri Lanka, central and west India, and Bangladesh.

5. Discussion

While we show that at least some of the CMIP6 GCMs used here do a reasonable job in simulating certain LPS statistics

and their structure, it is clear that important mechanisms are missing—e.g., coupling of the land surface to convection via heat fluxes (Deoras et al. 2025) and coupling of convective-scale updrafts to the large-scale circulation via vortex stretching and frictional convergence (Menon et al. 2025, manuscript submitted to *Quart. J. Roy. Meteor. Soc.*)—for which we require convection-permitting models. This is most acutely highlighted by the underestimation of LPS precipitation by about 20% in CMIP6 models compared to reanalyses. Combined, therefore, we should be very cautious about the specific values ascribed to projected changes in per-LPS precipitation. However, given the strength of the signal and the underlying thermodynamic arguments, we can be confident that the projected sign of the trend is correct.

In particular, GCMs significantly underestimate the interannual variability of LPS frequency. This may be due to poor representation of the BSISO (Abatan et al. 2021; Konda and Vissa 2022) or other important teleconnections such as with ENSO (Lin et al. 2024). We have shown that intermodel variability plays an important role, especially in, e.g., the frequency and inland penetration of LPSs. These relationships need to be explored in more detail in CMIP6 models in future work and would require more large ensemble data to be available at 6-hourly resolution.

We have also not addressed the sensitivity of our results to the arbitrary thresholds applied to the tracking algorithm, wherein LPSs had to reach a certain intensity, produce a certain amount of precipitation, and travel a certain distance to be included in our samples. These thresholds were drawn from the literature, and our results broadly agree with previous studies and observations. This sensitivity may be important when considering the behavior of weak LPSs, which make up much of the population. For example, a higher intensity threshold would have excluded many such systems and may have led to a different conclusion that the frequency of LPSs is projected to decline. Regardless, the more important conclusion that LPS activity (i.e., the combination of intensity and frequency) is projected to fall significantly is consistent with earlier studies and unlikely to be sensitive to the tracking thresholds.

6. Conclusions

In this study, we track monsoon LPSs in a large range of CMIP6 models in both historical and future climate scenarios. We assess model ability by comparing core LPS statistics—frequency, location, intensity, and precipitation—combined into a single metric, the "FLIP score," that we use as a weighting for multimodel means. We show that the FLIP score is a strong function of model resolution, with higher-resolution models performing much better.

The biggest impact of monsoon LPSs is their precipitation. Monsoon precipitation is projected to robustly increase with climate change, largely as a result of increased moisture availability, although the projected increase in overall monsoon precipitation is sub Clausius–Clapeyron (2%–3% K^{-1}) due to weakening dynamics and energy constraints (Doblas-Reyes et al. 2021). As LPSs are responsible for more than half of all monsoon precipitation, we expect LPS precipitation to increase, too. We show that this is indeed the case, corroborating many earlier studies. However, we also find that this relationship is complicated: There is superC-C scaling to the west of LPSs and subC-C scaling to the east. Furthermore, LPSs are also projected to weaken in intensity, as measured by their vorticity. We argue that these effects are driven by the following projected changes:

- a significant increase in the meridional gradient of lower-tropospheric specific humidity;
- an increase in the strength of frictional convergence in the boundary layer, relative to LPS intensity;
- and the continued importance of positive feedbacks within LPSs, e.g., through convection-driven vortex stretching.

We argue that these changes will also lead to a superC-C scaling of extreme rainfall within LPSs, which account for almost all extreme monsoon rainfall events (Thomas et al. 2021).

Previous studies have agreed on a projected reduction to LPS activity, i.e., a decline in seasonal mean kinetic energy, either through fewer systems, fewer stronger systems, or weakened mean intensity. Here, we argue that decline is predominantly manifested through weakened LPS intensity. In particular, lows (weaker LPSs) become much weaker, whereas depressions (stronger LPSs) appear to stay about the same. For a change in global warming level from 0° to 3°C, the weakest pentile of LPSs is projected to further decline in intensity by about 14%, compared with only 1% for the strongest pentile. This effect is not captured in models with a poor FLIP score. We argue that the weakened LPS intensity arises due to reduced barotropic instability over the Bay of Bengal, the region where most LPSs intensify. However, we also find increased barotropic instability over central India and the Arabian Sea, leading to deeper inland penetration of LPSs, with potentially large impacts for populated areas of east India. There is a significant increase in inland penetration (measured using postlandfall duration) between 1.5° and 2°C.

However, we also argue that LPS penetration is strongly subject to model uncertainty, as is LPS frequency. We are able to explain much of this variability using a storylines approach, where we cluster all model scenario years at 2°C on their anomalous 850-hPa u and v winds and specific humidity. We derive four diverse clusters, though all show the important increased meridional gradient in low-level moisture. For example, cluster 1 represents an extreme change with considerably more specific humidity and considerably weaker monsoon circulation than the other clusters. This leads to much weaker LPSs but with a very large increase in their precipitation (17%). In this cluster, there is a significant reduction in track density over the Bay of Bengal, which is compensated by increases to the north and south. Cluster 4 has enhanced easterlies over Southeast Asia and the Bay of Bengal and as such is able to transport many more LPS precursor vortices into the basin, thus giving the largest increase in LPS frequency (36%). Clusters 2 and 3 are most common (comprising 67% of

the total population) and represent slight shifting and weakening of monsoon circulation. All clusters agree to some extent on a deeper inland penetration of LPSs, so regardless of the future of the monsoon, there will be substantial impacts for west India. These impacts have already started to appear in observations (Kumari et al. 2025).

Acknowledgments. K. M. R. H. is supported by a NERC Independent Research Fellowship (MITRE; NE/W007924/1). A. G. T. is supported by the NERC International Programmes Award (NE/X006263/1).

Data availability statement. The LPS track data created during this study are freely available at https://doi.org/10.5281/zenodo.15829234.

REFERENCES

Abatan, A. A., M. Collins, M. S. Babel, D. Khadka, and Y. K. De Silva, 2021: Assessment of the ability of CMIP6 GCMS to simulate the boreal summer intraseasonal oscillation over Southeast Asia. *Front. Climate*, **3**, 716129, https://doi.org/10.3389/fclim.2021.716129.

Adames, Á. F., 2021: Interactions between water vapor, potential vorticity, and vertical wind shear in quasi-geostrophic motions: Implications for rotational tropical motion systems. *J. Atmos. Sci.*, **78**, 903–923, https://doi.org/10.1175/JAS-D-20-0205.1.

——, and Y. Ming, 2018: Interactions between water vapor and potential vorticity in synoptic-scale monsoonal disturbances: Moisture vortex instability. *J. Atmos. Sci.*, **75**, 2083–2106, https://doi.org/10.1175/JAS-D-17-0310.1.

Ashfaq, M., D. Rastogi, R. Mei, D. Touma, and L. Ruby Leung, 2017: Sources of errors in the simulation of South Asian summer monsoon in the CMIP5 GCMs. *Climate Dyn.*, **49**, 193–223, https://doi.org/10.1007/s00382-016-3337-7.

Ashrit, R. G., H. Douville, and K. R. Kumar, 2003: Response of the Indian monsoon and ENSO-monsoon teleconnection to enhanced greenhouse effect in the CNRM coupled model. *J. Meteor. Soc. Japan*, **81**, 779–803, https://doi.org/10.2151/jmsj.81.779.

Baldissera Pacchetti, M., L. Coulter, S. Dessai, T. G. Shepherd, J. Sillmann, and B. Van Den Hurk, 2024: Varieties of approaches to constructing physical climate storylines: A review. *Wiley Interdiscip. Rev.: Climate Change*, **15**, e869, https://doi.org/10.1002/wcc.869.

Baulenas, E., G. Versteeg, M. Terrado, J. Mindlin, and D. Bojovic, 2023: Assembling the climate story: Use of storyline approaches in climate-related science. *Global Challenges*, **7**, 2200183, https://doi.org/10.1002/gch2.202200183.

Bhattacharyya, S., S. Sreekesh, and A. King, 2022: Characteristics of extreme rainfall in different gridded datasets over India during 1983–2015. *Atmos. Res.*, **267**, 105930, https://doi.org/10.1016/j.atmosres.2021.105930.

Bhave, A. G., D. Conway, S. Dessai, and D. A. Stainforth, 2018: Water resource planning under future climate and socioeconomic uncertainty in the Cauvery River basin in Karnataka, India. *Water Resour. Res.*, **54**, 708–728, https://doi.org/10.1002/2017WR020970.

Bollasina, M. A., Y. Ming, and V. Ramaswamy, 2011: Anthropogenic aerosols and the weakening of the South Asian summer monsoon. *Science*, **334**, 502–505, https://doi.org/10.1126/science.1204994.

Chang, H.-I., D. Niyogi, A. Kumar, C. M. Kishtawal, J. Dudhia, F. Chen, U. C. Mohanty, and M. Shepherd, 2009: Possible relation between land surface feedback and the post-landfall structure of monsoon depressions. *Geophys. Res. Lett.*, **36**, L15826, https://doi.org/10.1029/2009GL037781.

Chen, D., and Coauthors, 2021: Framing, context, and methods. *Climate Change 2021: The Physical Science Basis*, V. Masson-Delmotte et al., Eds., Cambridge University Press, 147–286, https://doi.org/10.1017/9781009157896.003.

Chen, T.-C., and S.-P. Weng, 1999: Interannual and intraseasonal variations in monsoon depressions and their westward-propagating predecessors. *Mon. Wea. Rev.*, **127**, 1005–1020, https://doi.org/10.1175/1520-0493(1999)127<1005:IAIVIM>2.0.CO;2.

Chen, Z., T. Zhou, L. Zhang, X. Chen, W. Zhang, and J. Jiang, 2020: Global land monsoon precipitation changes in CMIP6 projections. *Geophys. Res. Lett.*, **47**, e2019GL086902, https://doi.org/10.1029/2019GL086902.

Cohen, N. Y., and W. R. Boos, 2014: Has the number of Indian summer monsoon depressions decreased over the last 30 years? *Geophys. Res. Lett.*, **41**, 7846–7853, https://doi.org/10.1002/2014GL061895.

Dash, S. K., J. R. Kumar, and M. S. Shekhar, 2004: On the decreasing frequency of monsoon depressions over the Indian region. *Curr. Sci.*, **86**, 1404–1410.

Deoras, A., K. M. R. Hunt, and A. G. Turner, 2021: The four regional varieties of South Asian monsoon low-pressure systems and their modulation by tropical intraseasonal variability. *Weather*, **76**, 194–200, https://doi.org/10.1002/wea.3997.

——, ——, and ——, 2025: The role of soil moisture in the inland penetration of Indian monsoon low-pressure systems. *Quart. J. Roy. Meteor. Soc.*, in press.

Dessai, S., A. Bhave, C. Birch, D. Conway, L. Garcia-Carreras, J. P. Gosling, N. Mittal, and D. Stainforth, 2018: Building narratives to characterise uncertainty in regional climate change through expert elicitation. *Environ. Res. Lett.*, **13**, 074005, https://doi.org/10.1088/1748-9326/aabcdd.

Diaz, M., and W. R. Boos, 2019: Monsoon depression amplification by moist barotropic instability in a vertically sheared environment. *Quart. J. Roy. Meteor. Soc.*, **145**, 2666–2684, https://doi.org/10.1002/qj.3585.

——, and ——, 2021: Evolution of idealized vortices in monsoon-like shears: Application to monsoon depressions. *J. Atmos. Sci.*, **78**, 1207–1225, https://doi.org/10.1175/JAS-D-20-0286.1.

Doblas-Reyes, F. J., and Coauthors, 2021: Linking global to regional climate change. *Climate Change 2021: The Physical Science Basis*, Cambridge University Press, 1363–1512, https://doi.org/10.1017/9781009157896.012.

Dong, W., Y. Ming, and V. Ramaswamy, 2020: Projected changes in South Asian monsoon low pressure systems. *J. Climate*, **33**, 7275–7287, https://doi.org/10.1175/JCLI-D-20-0168.1.

Eyring, V., S. Bony, G. A. Meehl, C. A. Senior, B. Stevens, R. J. Stouffer, and K. E. Taylor, 2016: Overview of the Coupled Model Intercomparison Project Phase 6 (CMIP6) experimental design and organization. *Geosci. Model Dev.*, **9**, 1937–1958, https://doi.org/10.5194/gmd-9-1937-2016.

Gelaro, R., and Coauthors, 2017: The Modern-Era Retrospective Analysis for Research and Applications, version 2 (MERRA-2). *J. Climate*, **30**, 5419–5454, https://doi.org/10.1175/JCLI-D-16-0758.1.

Godbole, R. V., 1977: The composite structure of the monsoon depression. *Tellus*, **29** (1), 25–40, https://doi.org/10.1111/j.2153-3490.1977.tb00706.x.

Goswami, B. N., R. N. Keshavamurty, and V. Satyan, 1980: Role of barotropic, baroclinic and combined barotropic-baroclinic instability for the growth of monsoon depressions and midtropospheric cyclones. *Proc. Indian Acad. Sci. Earth Planet. Sci.*, **89**, 79–97, https://doi.org/10.1007/BF02841521.

Held, I. M., and B. J. Soden, 2006: Robust responses of the hydrological cycle to global warming. *J. Climate*, **19**, 5686–5699, https://doi.org/10.1175/JCLI3990.1.

Hersbach, H., and Coauthors, 2020: The ERA5 global reanalysis. *Quart. J. Roy. Meteor. Soc.*, **146**, 1999–2049, https://doi.org/10.1002/qj.3803.

Hunt, K. M. R., and A. G. Turner, 2017: The effect of soil moisture perturbations on Indian monsoon depressions in a numerical weather prediction model. *J. Climate*, **30**, 8811–8823, https://doi.org/10.1175/JCLI-D-16-0733.1.

——, and J. K. Fletcher, 2019: The relationship between Indian monsoon rainfall and low-pressure systems. *Climate Dyn.*, **53**, 1859–1871, https://doi.org/10.1007/s00382-019-04744-x.

——, and A. G. Turner, 2022: Non-linear intensification of monsoon low-pressure systems by the BSISO. *Wea. Climate Dyn.*, **3**, 1341–1358, https://doi.org/10.5194/wcd-3-1341-2022.

——, and ——, 2024: Using interpretable gradient-boosted decision-tree ensembles to uncover novel dynamical relationships governing monsoon low-pressure systems. *Quart. J. Roy. Meteor. Soc.*, **150** (758), 1–24, https://doi.org/10.1002/qj.4582.

——, and S. P. Harrison, 2025: A novel explainable deep learning framework for reconstructing South Asian palaeomonsoons. *Climate Past*, **21** (1), 1–26, https://doi.org/10.5194/cp-21-1-2025.

——, A. G. Turner, P. M. Inness, D. E. Parker, and R. C. Levine, 2016a: On the structure and dynamics of Indian monsoon depressions. *Mon. Wea. Rev.*, **144**, 3391–3416, https://doi.org/10.1175/MWR-D-15-0138.1.

——, ——, and D. E. Parker, 2016b: The spatiotemporal structure of precipitation in Indian monsoon depressions. *Quart. J. Roy. Meteor. Soc.*, **142**, 3195–3210, https://doi.org/10.1002/qj.2901.

Hurley, J. V., and W. R. Boos, 2015: A global climatology of monsoon low-pressure systems. *Quart. J. Roy. Meteor. Soc.*, **141**, 1049–1064, https://doi.org/10.1002/qj.2447.

Jiang, J., and T. Zhou, 2019: Global monsoon responses to decadal sea surface temperature variations during the twentieth century: Evidence from AGCM simulations. *J. Climate*, **32**, 7675–7695, https://doi.org/10.1175/JCLI-D-18-0890.1.

Katzenberger, A., J. Schewe, J. Pongratz, and A. Levermann, 2021: Robust increase of Indian monsoon rainfall and its variability under future warming in CMIP6 models. *Earth Syst. Dyn.*, **12**, 367–386, https://doi.org/10.5194/esd-12-367-2021.

Kishtawal, C. M., D. Niyogi, B. Rajagopalan, M. Rajeevan, N. Jaiswal, and U. C. Mohanty, 2013: Enhancement of inland penetration of monsoon depressions in the Bay of Bengal due to prestorm ground wetness. *Water Resour. Res.*, **49**, 3589–3600, https://doi.org/10.1002/wrcr.20301.

Kitoh, A., H. Endo, K. Krishna Kumar, I. F. Cavalcanti, P. Goswami, and T. Zhou, 2013: Monsoons in a changing world: A regional perspective in a global context. *J. Geophys. Res. Atmos.*, **118**, 3053–3065, https://doi.org/10.1002/jgrd.50258.

Konda, G., and N. K. Vissa, 2022: Robustness of BSISO and air-sea interactions in the CMIP (Phase-6) models over the North Indian Ocean. *Dyn. Atmos. Oceans*, **99**, 101316, https://doi.org/10.1016/j.dynatmoce.2022.101316.

Krishnamurthy, V., and R. S. Ajayamohan, 2010: Composite structure of monsoon low pressure systems and its relation to Indian rainfall. *J. Climate*, **23**, 4285–4305, https://doi.org/10.1175/2010JCLI2953.1.

Kumari, A., R. Attada, J. S. Chowdary, N. Mahendra, N. Chilukoti, and R. K. Karumuri, 2025: Recent decades witness a strong east-west gradient of monsoon precipitation changes over Northern India. *Atmos. Res.*, **318**, 108014, https://doi.org/10.1016/j.atmosres.2025.108014.

Lau, W. K.-M., and K.-M. Kim, 2017: Competing influences of greenhouse warming and aerosols on Asian summer monsoon circulation and rainfall. *Asia. Pac. J. Atmos. Sci.*, **53**, 181–194, https://doi.org/10.1007/s13143-017-0033-4.

Levine, R. C., and G. M. Martin, 2018: On the climate model simulation of Indian monsoon low pressure systems and the effect of remote disturbances and systematic biases. *Climate Dyn.*, **50**, 4721–4743, https://doi.org/10.1007/s00382-017-3900-x.

Lin, S., B. Dong, S. Yang, and T. Zhang, 2024: Diverse impacts of the Indian summer monsoon on ENSO among CMIP6 models and its possible causes. *Environ. Res. Lett.*, **19**, 084052, https://doi.org/10.1088/1748-9326/ad6618.

Luo, H., Á. F. Adames Corraliza, and R. B. Rood, 2023: Barotropic and moisture–vortex growth of monsoon low pressure systems. *J. Atmos. Sci.*, **80**, 2823–2836, https://doi.org/10.1175/JAS-D-22-0252.1.

Mahto, S. S., and V. Mishra, 2019: Does ERA-5 outperform other reanalysis products for hydrologic applications in India? *J. Geophys. Res. Atmos.*, **124**, 9423–9441, https://doi.org/10.1029/2019JD031155.

Martin, G. M., and Coauthors, 2020: Forecasting the monsoon on daily to seasonal time-scales in support of a field campaign. *Quart. J. Roy. Meteor. Soc.*, **146**, 2906–2927, https://doi.org/10.1002/qj.3620.

Masson-Delmotte, V., and Coauthors, Eds., 2018: *Global Warming of 1.5°C.* Intergovernmental Panel on Climate Change, 616 pp., https://www.ipcc.ch/sr15/.

May, W., 2004: Simulation of the variability and extremes of daily rainfall during the Indian summer monsoon for present and future times in a global time-slice experiment. *Climate Dyn.*, **22**, 183–204, https://doi.org/10.1007/s00382-003-0373-x.

Meera, M., E. Suhas, and S. Sandeep, 2019: Downstream and in situ: Two perspectives on the initiation of monsoon low-pressure systems over the Bay of Bengal. *Geophys. Res. Lett.*, **46**, 12 303–12 310, https://doi.org/10.1029/2019GL084555.

Monerie, P.-A., M. Biasutti, J. Mignot, E. Mohino, B. Pohl, and G. Zappa, 2023: Storylines of Sahel precipitation change: Roles of the North Atlantic and Euro-Mediterranean temperature. *J. Geophys. Res. Atmos.*, **128**, e2023JD038712, https://doi.org/10.1029/2023JD038712.

Moon, S., and K.-J. Ha, 2020: Future changes in monsoon duration and precipitation using CMIP6. *npj Climate Atmos. Sci.*, **3**, 45, https://doi.org/10.1038/s41612-020-00151-w.

Moorthi, S., and A. Arakawa, 1985: Baroclinic instability with cumulus heating. *J. Atmos. Sci.*, **42**, 2007–2031, https://doi.org/10.1175/1520-0469(1985)042<2007:BIWCH>2.0.CO;2.

O'Neill, B. C., and Coauthors, 2016: The Scenario Model Intercomparison Project (ScenarioMIP) for CMIP6. *Geosci. Model Dev.*, **9**, 3461–3482, https://doi.org/10.5194/gmd-9-3461-2016.

Paul, S., and H. Alemohammad, 2025: Examining the performance of precipitation products in characterizing the Indian summer

monsoon rainfall (ISMR) using triple collocation. *J. Hydrol.*, **657**, 133136, https://doi.org/10.1016/j.jhydrol.2025.133136.

Prabhu, S., and V. Chitale, 2024: Decoding India's changing monsoon patterns: A Tehsil-level assessment. Council on Energy, Environment and Water Tech. Rep., 48 pp., https://www.ceew.in/publications/decoding-changing-monsoon-rainfall-patterns-due-to-climate-change-in-india.

Prajeesh, A. G., K. Ashok, and D. V. Bhaskar Rao, 2013: Falling monsoon depression frequency: A Gray-Sikka conditions perspective. *Sci. Rep.*, **3**, 2989, https://doi.org/10.1038/srep02989.

Rajamani, S., and K. V. Rao, 1981: On the occurrence of rainfall over southwest sector of monsoon depression. *Mausam*, **32**, 215–220, https://doi.org/10.54302/mausam.v32i3.3367.

——, and D. N. Sikdar, 1989: Some dynamical characteristics and thermal structure of monsoon depressions over the Bay of Bengal. *Tellus*, **41A**, 255–269, https://doi.org/10.3402/tellusa.v41i3.11838.

Rastogi, D., M. Ashfaq, L. R. Leung, S. Ghosh, A. Saha, K. Hodges, and K. Evans, 2018: Characteristics of Bay of Bengal monsoon depressions in the 21st century. *Geophys. Res. Lett.*, **45**, 6637–6645, https://doi.org/10.1029/2018GL078756.

Roy, P., and T. N. Rao, 2022: Precipitation characteristics of cyclonic disturbances over the South Asia region as revealed by TRMM and GPM. *J. Climate*, **35**, 4943–4957, https://doi.org/10.1175/JCLI-D-21-0774.1.

Saha, K., F. Sanders, and J. Shukla, 1981: Westward propagating predecessors of monsoon depressions. *Mon. Wea. Rev.*, **109**, 330–343, https://doi.org/10.1175/1520-0493(1981)109<0330:WPPOMD>2.0.CO;2.

Samset, B. H., M. T. Lund, M. Bollasina, G. Myhre, and L. Wilcox, 2019: Emerging Asian aerosol patterns. *Nat. Geosci.*, **12**, 582–584, https://doi.org/10.1038/s41561-019-0424-5.

Sandeep, S., R. S. Ajayamohan, W. R. Boos, T. P. Sabin, and V. Praveen, 2018: Decline and poleward shift in Indian summer monsoon synoptic activity in a warming climate. *Proc. Natl. Acad. Sci. USA*, **115**, 2681–2686, https://doi.org/10.1073/pnas.1709031115.

Shepherd, T. G., and Coauthors, 2018: Storylines: An alternative approach to representing uncertainty in physical aspects of climate change. *Climate Change*, **151**, 555–571, https://doi.org/10.1007/s10584-018-2317-9.

Shi, H., B. Wang, E. R. Cook, J. Liu, and F. Liu, 2018: Asian summer precipitation over the past 544 years reconstructed by merging tree rings and historical documentary records. *J. Climate*, **31**, 7845–7861, https://doi.org/10.1175/JCLI-D-18-0003.1.

Sikka, D. R., 2006: *A Study on the Monsoon Low Pressure Systems over the Indian Region and their Relationship with Drought and Excess Monsoon Seasonal Rainfall.* Center for Ocean-Land-Atmosphere Studies, Center for the Application of Research on the Environment, 61 pp.

Sontakke, N. A., N. Singh, and H. N. Singh, 2008: Instrumental period rainfall series of the Indian region (AD 1813—2005): Revised reconstruction, update and analysis. *Holocene*, **18**, 1055–1066, https://doi.org/10.1177/0959683608095576.

Sørland, S. L., A. Sorteberg, C. Liu, and R. Rasmussen, 2016: Precipitation response of monsoon low-pressure systems to an idealized uniform temperature increase. *J. Geophys. Res. Atmos.*, **121**, 6258–6272, https://doi.org/10.1002/2015JD024658.

Sperber, K. R., H. Annamalai, I.-S. Kang, A. Kitoh, A. Moise, A. Turner, B. Wang, and T. Zhou, 2013: The Asian summer monsoon: An intercomparison of CMIP5 vs. CMIP3 simulations of the late 20th century. *Climate Dyn.*, **41**, 2711–2744, https://doi.org/10.1007/s00382-012-1607-6.

Srujan, K. S. S. S., S. Sandeep, and E. Suhas, 2021: Downstream and in situ genesis of monsoon low-pressure systems in climate models. *Earth Space Sci.*, **8**, e2021EA001741, https://doi.org/10.1029/2021EA001741.

Stano, G., T. N. Krishnamurti, T. S. V. Vijaya Kumar, and A. Chakraborty, 2002: Hydrometeor structure of a composite monsoon depression using the TRMM radar. *Tellus*, **54A**, 370–381, https://doi.org/10.3402/tellusa.v54i4.12154.

Suhas, D. L., and W. R. Boos, 2023: Monsoon depression amplification by horizontal shear and humidity gradients: A shallow water perspective. *J. Atmos. Sci.*, **80**, 633–647, https://doi.org/10.1175/JAS-D-22-0146.1.

——, N. Ramesh, R. M. Kripa, and W. R. Boos, 2023: Influence of monsoon low pressure systems on South Asian disasters and implications for disaster prediction. *npj Climate Atmos. Sci.*, **6**, 48, https://doi.org/10.1038/s41612-023-00376-5.

Thomas, T. M., G. Bala, and V. V. Srinivas, 2021: Characteristics of the monsoon low pressure systems in the Indian subcontinent and the associated extreme precipitation events. *Climate Dyn.*, **56**, 1859–1878, https://doi.org/10.1007/s00382-020-05562-2.

——, ——, and S. V. Vemavarapu, 2022a: CESM simulation of monsoon low pressure systems over India. *Int. J. Climatol.*, **42**, 5964–5984, https://doi.org/10.1002/joc.7571.

——, ——, and V. Vemavarapu Srinivas, 2022b: Change in characteristics of monsoon low pressure systems under a warming climate. *EGU General Assembly*, Vienna, Austria, European Geosciences Union, Abstract EGU22-1006.

Vishnu, S., P. A. Francis, S. S. C. Shenoi, and S. S. V. S. Ramakrishna, 2016: On the decreasing trend of the number of monsoon depressions in the Bay of Bengal. *Environ. Res. Lett.*, **11**, 014011, https://doi.org/10.1088/1748-9326/11/1/014011.

——, W. R. Boos, P. A. Ullrich, and T. A. O'Brien, 2020: Assessing historical variability of South Asian monsoon lows and depressions with an optimized tracking algorithm. *J. Geophys. Res. Atmos.*, **125**, e2020JD032977, https://doi.org/10.1029/2020JD032977.

——, ——, and W. D. Collins, 2023: Historical and future trends in South Asian monsoon low pressure systems in a high-resolution model ensemble. *npj Climate Atmos. Sci.*, **6**, 182, https://doi.org/10.1038/s41612-023-00502-3.

Wang, B., C. Jin, and J. Liu, 2020: Understanding future change of global monsoons projected by CMIP6 models. *J. Climate*, **33**, 6471–6489, https://doi.org/10.1175/JCLI-D-19-0993.1.

——, and Coauthors, 2021: Monsoons climate change assessment. *Bull. Amer. Meteor. Soc.*, **102**, E1–E19, https://doi.org/10.1175/BAMS-D-19-0335.1.

You, Y., and M. Ting, 2021: Observed trends in the South Asian monsoon low-pressure systems and rainfall extremes since the late 1970s. *Geophys. Res. Lett.*, **48**, e2021GL092378, https://doi.org/10.1029/2021GL092378.

Zappa, G., and T. G. Shepherd, 2017: Storylines of atmospheric circulation change for European regional climate impact assessment. *J. Climate*, **30**, 6561–6577, https://doi.org/10.1175/JCLI-D-16-0807.1.